Atmos. Chem. Phys., 17, 5947–5972, 2017
www.atmos-chem-phys.net/17/5947/2017/
doi:10.5194/acp-17-5947-2017

Atmospheric Chemistry and Physics Open Access EGU

Derivation of aerosol profiles for MC3E convection studies and use in simulations of the 20 May squall line case

Ann M. Fridlind[1], Xiaowen Li[2,3], Di Wu[3,4], Marcus van Lier-Walqui[1,5], Andrew S. Ackerman[1], Wei-Kuo Tao[3], Greg M. McFarquhar[6], Wei Wu[6], Xiquan Dong[7], Jingyu Wang[7], Alexander Ryzhkov[8], Pengfei Zhang[8], Michael R. Poellot[9], Andrea Neumann[9], and Jason M. Tomlinson[10]

[1]NASA Goddard Institute for Space Studies, 2880 Broadway, New York, NY, USA
[2]Goddard Earth Sciences Technology and Research, Morgan State University, Baltimore, MD, USA
[3]Mesoscale Atmospheric Processes Laboratory, NASA Goddard Space Flight Center, Greenbelt, MD, USA
[4]Science Systems and Applications, Inc., Lanham, MD, USA
[5]Center for Climate Systems Research, Columbia University, New York, NY, USA
[6]Department of Atmospheric Sciences, University of Illinois, Urbana-Champaign, IL, USA
[7]Department of Hydrology and Atmospheric Sciences, University of Arizona, Tucson, AZ, USA
[8]Cooperative Institute for Mesoscale Meteorological Studies, University of Oklahoma, and National Severe Storms Laboratory, Norman, OK, USA
[9]Department of Atmospheric Sciences, University of North Dakota, Grand Forks, ND, USA
[10]Pacific Northwest National Laboratory, Richland, WA, USA

Correspondence to: Ann M. Fridlind (ann.fridlind@nasa.gov)

Received: 24 October 2016 – Discussion started: 14 November 2016
Revised: 3 April 2017 – Accepted: 17 April 2017 – Published: 15 May 2017

Abstract. Advancing understanding of deep convection microphysics via mesoscale modeling studies of well-observed case studies requires observation-based aerosol inputs. Here, we derive hygroscopic aerosol size distribution input profiles from ground-based and airborne measurements for six convection case studies observed during the Midlatitude Continental Convective Cloud Experiment (MC3E) over Oklahoma. We demonstrate use of an input profile in simulations of the only well-observed case study that produced extensive stratiform outflow on 20 May 2011. At well-sampled elevations between -11 and $-23\,^{\circ}$C over widespread stratiform rain, ice crystal number concentrations are consistently dominated by a single mode near $\sim 400\,\mu$m in randomly oriented maximum dimension ($D_{\max}$). The ice mass at $-23\,^{\circ}$C is primarily in a closely collocated mode, whereas a mass mode near $D_{\max} \sim 1000\,\mu$m becomes dominant with decreasing elevation to the $-11\,^{\circ}$C level, consistent with possible aggregation during sedimentation. However, simulations with and without observation-based aerosol inputs systematically overpredict mass peak $D_{\max}$ by a factor of 3–5 and underpredict ice number concentration by a factor of 4–10. Previously reported simulations with both two-moment and size-resolved microphysics have shown biases of a similar nature. The observed ice properties are notably similar to those reported from recent tropical measurements. Based on several lines of evidence, we speculate that updraft microphysical pathways determining outflow properties in the 20 May case are similar to a tropical regime, likely associated with warm-temperature ice multiplication that is not well understood or well represented in models.

1 Introduction

The impacts of hygroscopic, absorbing, and ice-nucleating aerosols on deep convection have been the subject of intensive study using both observational and modeling approaches, as summarized in several recent reviews (e.g., Tao et al., 2012; Wang, 2013; Altaratz et al., 2014). A hindrance for the modeling studies is the widely reported finding that different advanced microphysics schemes, given the same environmental conditions and setup, often predict substan-

tially differing results in terms of ice mass mixing ratios and other cloud properties (e.g., Zhu et al., 2012; Van Weverberg et al., 2013; Fan et al., 2015; Wang et al., 2015b; Tao et al., 2016). Microphysics schemes give such diverse results at least in part owing to the complexity of updraft microphysics and a paucity of existing field and laboratory data adequate to constrain all of the relevant physical processes and parameters (e.g., Zeng et al., 2011; Varble et al., 2014a).

An objective for the representation of convective microphysics in climate models is the realistic representation of the relatively long-lived convective outflow that may substantially impact global radiative budgets, circulation, and climate sensitivity (e.g., Houze, 2004; Schumacher et al., 2004; Mauritsen and Stevens, 2015; Donner et al., 2016; Elsaesser et al., 2017). Using the Cloud-Associated Parameterization Testbed (CAPT) approach to study simulation of deep convection by nine global models in various configurations, Lin et al. (2012) found that models produced grossly differing stratiform heating profiles. In a comparison of cloud-resolving simulations using a range of dynamic cores and microphysics schemes under similar conditions, Fridlind et al. (2012) found similarly pronounced differences in predicted stratiform outflow, with substantial associated impacts on radiative fluxes. Based on comparison of larger-domain convection-permitting simulations with tropical satellite data, Van Weverberg et al. (2013) concluded that such simulations are sensitive to microphysics parameterizations and that more complex schemes do not necessarily perform better. Evidence from recent tropical field measurements has indicated that microphysics schemes could be failing to represent efficient ice multiplication that may strongly impact tropical updraft glaciation rate, outflow ice size, and precipitation efficiency (Ackerman et al., 2015), providing further motivation to advance fundamental knowledge of updraft microphysical pathways. Owing to the challenging complexity of coupled dynamical and microphysical processes within outflow-generating updrafts and the increasing ability of computational approaches to resolve such coupling (e.g., Lebo and Morrison, 2015), the goal of improving understanding of deep convection processes through high-resolution simulation of well-observed case studies is increasingly attractive (e.g., Yang et al., 2015).

Establishing reliability of high-resolution simulations to advance fundamental knowledge of convective microphysics depends on observational constraint of initial conditions as well as simulation results. Whereas thermodynamic conditions may be well characterized by routine observations or reanalysis fields (e.g., Zhu et al., 2012), aerosol initial conditions for any observed case study generally require detailed observational inputs (e.g., Yang et al., 2015). Here, we develop hygroscopic aerosol input data sets for six convection events that were well observed during the Midlatitude Continental Convective Cloud Experiment (MC3E), a joint field program of the US Department of Energy Atmospheric Radiation Measurement (ARM) program and the NASA Global Precipitation Measurement Mission (Jensen et al., 2016). Aerosol input profiles are archived as Supplement 1. We also demonstrate use of derived aerosol input size distributions in simulations of the only event with extensive stratiform outflow that was well sampled by aircraft, on 20 May 2011 (Wang et al., 2015a; Wu and McFarquhar, 2016), with an emphasis on comparing simulated hydrometeor size distributions with observations.

In the following sections, we describe the selection of six convection case studies from the MC3E campaign (Sect. 2), derivation of aerosol specifications for each case from ground-based and aircraft measurements (Sect. 3), and comparison of simulated hydrometeor size distributions with observations for the 20 May case study (Sect. 4). Results are summarized and discussed in the context of other recent measurement campaigns and modeling studies (Sect. 5).

2 Case study selection

The MC3E domain (Fig. 1) is defined by a sounding array containing a triangular X-band radar array and a central facility with additional instruments, including a Ka-band ARM zenith radar (KAZR), a NOAA S-band (2.8 GHz) profiling radar, a TSI model 3010 condensation particle counter (CPC), a DMT model 1 cloud condensation nuclei (CCN) counter, and a humidified tandem differential mobility analyzer (HTDMA). We begin by focusing on the 22 April–25 May 2011 time period of MC3E for which a large-scale forcing data set was initially derived using a variational analysis approach (Jensen et al., 2015). During this time period, 10 flights of the University of North Dakota *Citation* aircraft provide profiles of aerosol properties to elevations of 8 km or higher (on 22, 25, and 27 April, and 1, 10, 11, 18, 20, 23, and 24 May). Aerosol number size distribution in the 0.06–1 µm diameter size range was measured on the *Citation* with an ultra-high sensitivity aerosol spectrometer (UHSAS) and the number concentration of aerosols with a diameter larger than 10 nm was measured with a TSI 3771 CPC.

Owing to the importance of identifying fine-scale convection structural features in simulations, we first select case studies when the C-band scanning ARM precipitation radar (C-SAPR) was fully or partly operational, which eliminates two flight dates (10 and 11 May). In order to allow simultaneous use of profiling instruments, we focus on cases in which substantial convection features passed directly over the KAZR and other nearby instruments at the central facility, which eliminates two more flight dates (22 April and 18 May). This leaves six flight dates for which aerosol property profiles are derived here for use in convection simulations: 25 and 27 April, and 1, 20, 23, and 24 May. Figure 2 illustrates the varying convection that passed over the central facility on each date, including the long duration of stratiform rain following deep convection in the 20 May case.

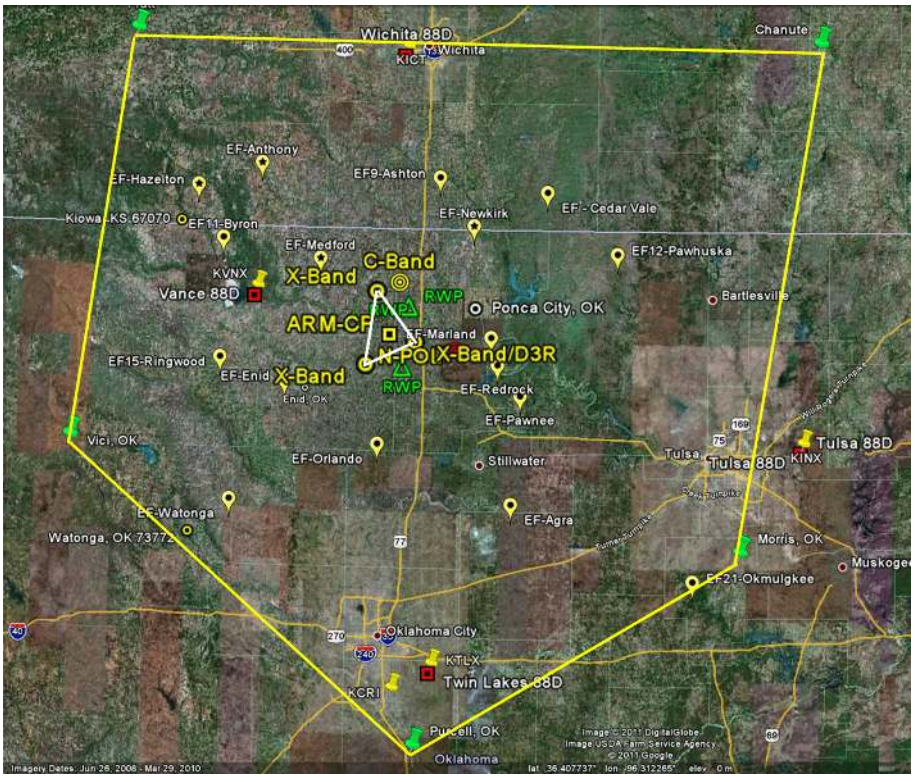

Figure 1. MC3E operations map: around the ARM central facility (small yellow square) are arrayed the X-band radars (white triangle), the sounding array (large yellow pentagon), and the C-band scanning ARM precipitation radar (C-SAPR) (yellow bullseye symbol); figure courtesy of Michael Jensen.

3 Aerosol input data

3.1 Objective

Based on evidence that aerosol consumption via droplet activation may be efficient in strong updrafts (e.g., Fridlind et al., 2004; Yang et al., 2015) and nanometer-sized particles could be nucleated (e.g., Ekman et al., 2006; Khain et al., 2012), emphasis is placed on deriving size distribution profiles that include aerosol of all available sizes for each case. Owing to lack of measurements, we unfortunately omit coarse-mode (supermicron) aerosol, which may constitute $\sim$ 1–10 cm^{-3} aerosol that is a small fraction of relevant hygroscopic aerosols but may be especially relevant to heterogeneous ice nucleation (DeMott et al., 2010; Corr et al., 2016). To make simulation specifications relatively simple, it is also assumed that a single size distribution profile will be used in each case (no time dependence of specified environmental aerosol conditions), as in past deep convection studies that have specified observation-based aerosol profiles (e.g., Barth et al., 2007; Fridlind et al., 2012; Yang et al., 2015).

3.2 Ground-based measurements

As shown in Fig. 3, the ground-based aerosol instrumentation operated continuously with few interruptions throughout the campaign. For each case study, a 2 h time period prior to the detection of surface precipitation at the central facility is first identified on each date (dotted vertical lines in Fig. 3). When averaging measurements over these pre-convection periods, we find that the total aerosol number concentration reported by the HTDMA (0.012–0.74 µm dry diameter) agrees with that reported by the ground-based CPC (0.01–3 µm) to within 30 % in all cases except 25 April and 1 May, when the HTDMA concentration is 80 % higher and 50 % lower, respectively. The reasons for disagreement are unclear; here, we will rely on the HTDMA data for size distribution information, while noting the discrepancy. Based on the discrepancy between ground-based CPC and HTDMA measurements, we estimate that overall uncertainty in derived total aerosol number concentrations is roughly a factor of 2 throughout this work.

The large variability of spread between CCN, HTDMA, and ground-based CPC measurements reflects the large variability in nucleation-mode aerosol concentrations. CCN data reported at the highest supersaturation measured (slightly above 1 %) variably account for roughly 15–80 % of the

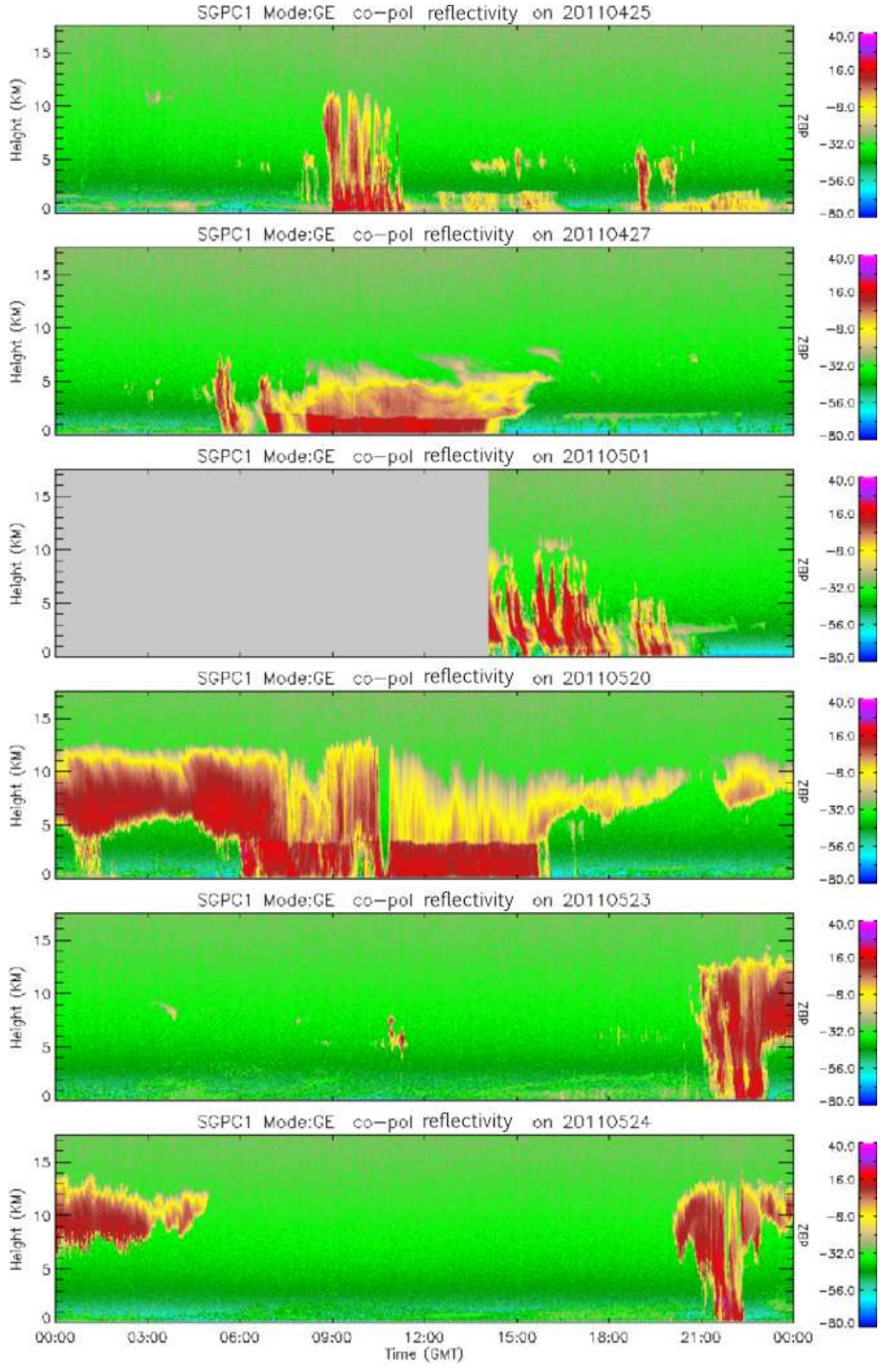

Figure 2. KAZR radar reflectivity at the central facility during six case studies that began on 25 and 27 April, and 1, 20, 23, and 24 May 2011.

aerosol reported by the ground-based CPC and range over nearly an order of magnitude ($\sim$ 400–3000 cm^{-3}) across the six case studies, with an intermediate value of $\sim$ 2000 cm^{-3} on 20 May.

Also shown in Fig. 3 is aerosol hygroscopicity parameter (κ) derived from HTDMA measurements, linearly averaged in six reported size ranges. Commonly low κ values of $\sim$ 0.1 are consistent with those derived from airborne aerosol size distribution and CCN measurements at a similar time of year over the Southern Great Plains site (Vogelmann et al., 2015). Similar to long-term measurements from the organic-rich Amazon rain forest (Pöhlker et al., 2016), there appears

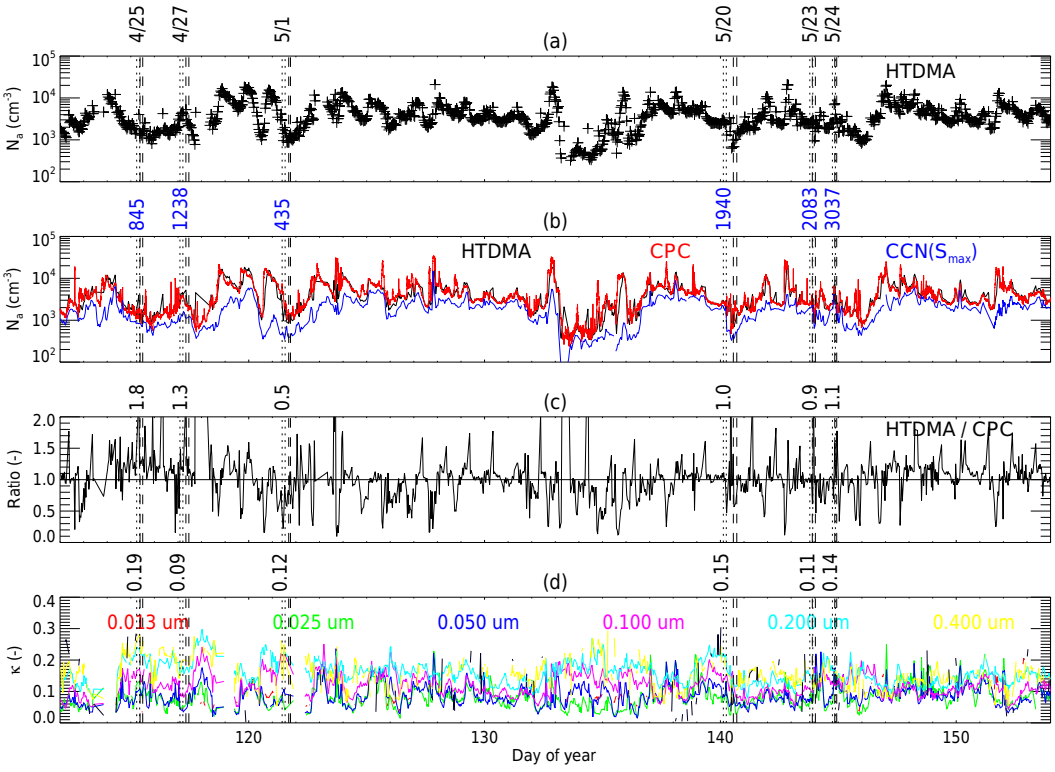

Figure 3. Ground-based aerosol properties at the central facility during MC3E: **(a)** total number concentration (N_a) measured by the HTDMA; **(b)** N_a measured by the HTDMA, ground-based CPC, and CCN at maximum supersaturation of approximately 1 %; **(c)** ratio of N_a measured by HTDMA to that measured by ground-based CPC; and **(d)** hygroscopicity parameter (κ) measured by the HTDMA at six sizes (intermittent at smallest cut). For each case study, pairs of dashed and dotted vertical lines bound the *Citation* flight duration and a 2 h pre-rain period, respectively; values above plots are pre-rain period averages, linearly averaged over available sizes for κ. Dates are indicated in m/dd format.

to be a common trend of increasing κ with size between the Aitken- and accumulation-mode size ranges.

3.3 Aircraft measurements

The MC3E aircraft measurements were commonly taken during precipitation at the ground site in order to sample cloud and precipitation conditions (see Fig. 3). We filter all aircraft aerosol measurements to remove in-cloud samples by imposing the stringent requirement that hydrometeors in the 2–50 µm diameter range measured by a cloud droplet probe (CDP) remain below the detection limit (cf. McFarquhar and Cober, 2004), which is roughly 0.03 cm^{-3} given the CDP sample area of 0.3 mm^2 (Lance et al., 2010) and a typical *Citation* aircraft speed of 100 m s^{-1}. Unfortunately, out of the six convection case studies considered here, UHSAS data were available only for the first three and airborne CPC data only for the latter three. After surveying the available airborne CPC and UHSAS data for the six case studies, we analyze aerosol measurements from all flight dates to provide estimates of missing information.

Out-of-cloud airborne CPC profiles measured on 20, 23, and 24 May indicate that nucleation-mode aerosols could be present in the region even when they were not detected at the ground site during the pre-convection period (Fig. 4). Based on the airborne CPC data available from twelve flights during MC3E, freshly nucleated particles were commonly associated with condensation nuclei concentrations in excess of 10^4 cm^{-3}, typically limited to or most concentrated below 1–3 km in altitude, and encountered during every flight except that on 23 May. Thus, even when not present at the ground site, as on 20 May, nucleation-mode particles were virtually always present somewhere nearby. However, aircraft data consistently indicated a high degree of variability in the distribution of nucleation-mode particles in the boundary layer. Maps of airborne CPC concentration, as a function of latitude and longitude on each flight, indicated that the nucleation mode was commonly limited to a short flight segment (not shown), indicative of transects through plumes likely generated by emissions from multiple nearby power plants that may not broaden efficiently downwind (e.g., Wang et al., 2006; Stevens et al., 2012). The airport could also be a source affecting the airborne samples (e.g., Westerdahl et al., 2008).

Out-of-cloud UHSAS profiles measured on 25 and 27 April and 1 May indicate median concentrations of 100–

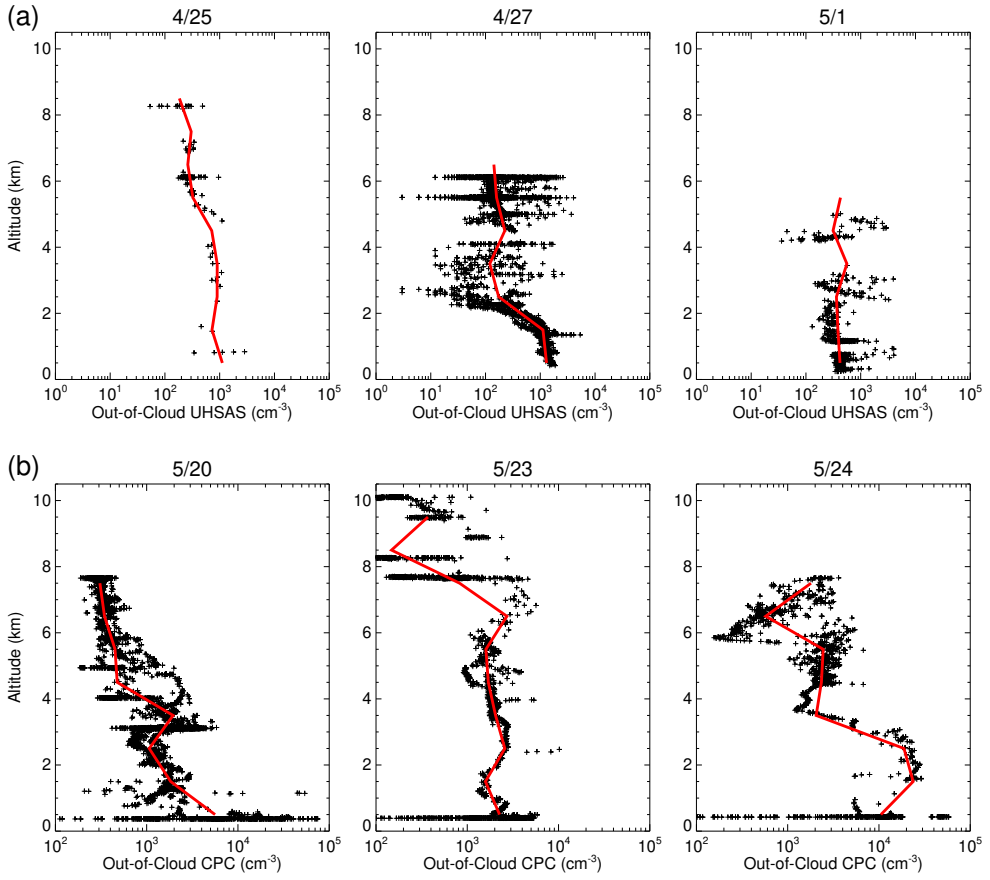

Figure 4. Out-of-cloud measurements of aerosol number concentration available on case study days (black symbols) from UHSAS **(a)** and airborne CPC **(b)** and median values over 1 km deep layers (red lines). Dates are indicated in m/dd format.

1000 cm $^{-3}$ commonly decreasing with increasing elevation (Fig. 4). On the latter two dates, long flight legs at a single elevation indicate horizontal variability commonly exceeding an order of magnitude both greater and lesser than relatively well-defined mean profiles.

Figure 5 shows profiles of median UHSAS and airborne CPC concentrations during all MC3E flights, as well as their ratio for the seven flights on which both instruments simultaneously functioned. UHSAS is shown to represent a fraction of airborne CPC that generally decreases with height above $\sim$2 km, consistent with the expectation that the surface is a source of the larger aerosol. However, the local minimum in the ratio of UHSAS to CPC seen at the surface is consistent with a surface source also for fine particles (e.g., Wang et al., 2006, their Fig. 7), which could be both spatiotemporally variable and regional in nature (e.g., Crippa and Pryor, 2013). Considering the general vertical trend of number concentration, median out-of-cloud UHSAS number concentration summed over 0.06–1.0 µm dry diameter accounts for 20–60 % of collocated median airborne CPC number concentration when taken over 1 km vertical layers during each flight. The campaign-wide median profiles of UHSAS and airborne CPC profiles and their ratio are archived as Supplement 2. Since each case study date offered only UHSAS or CPC but not both, the median ratio of UHSAS to airborne CPC number concentration shown in Fig. 5 is used as a guide for scaling ground-based measurements, which are derived as follows.

3.4 Derivation of hygroscopic aerosol input data

3.4.1 Below 1 km

Input profiles for each case study are derived at 1 km vertical resolution, owing to the commonality of relatively sparse aircraft data over some elevations. Ground-based measurements are used to define aerosol number size distribution and hygroscopicity in the 1 km layer at the surface. First, all HTDMA size distributions measured during each pre-convection period are fit with lognormal modes using the approach described by Vogelmann et al. (2015). The Vogelmann et al. (2015) algorithm optimizes a fit of two or three modes for each size distribution (Fig. 6). The mode properties are then averaged in time. In the case that three modes provided a best fit, those are each averaged by mode. In the case that only

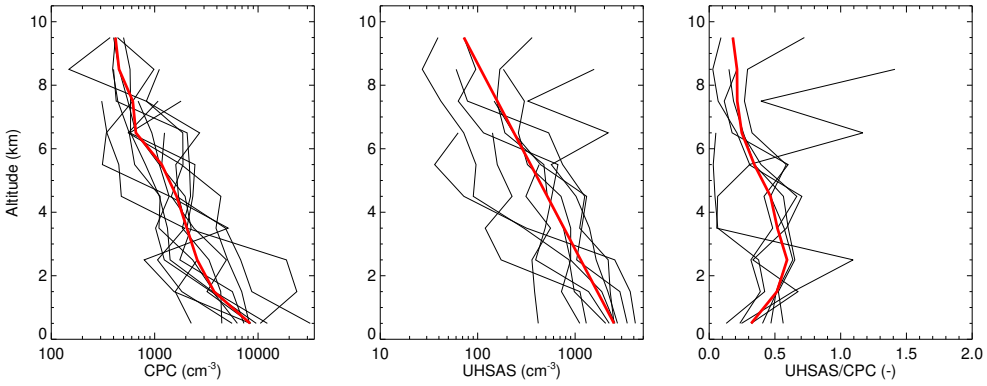

Figure 5. The median of airborne CPC and UHSAS aerosol number concentrations within 1 km deep layers for each MC3E flight, and the ratio of those median values for the seven flights with both instruments (black lines). The campaign-wide median profiles (red lines) are archived as Supplement 2.

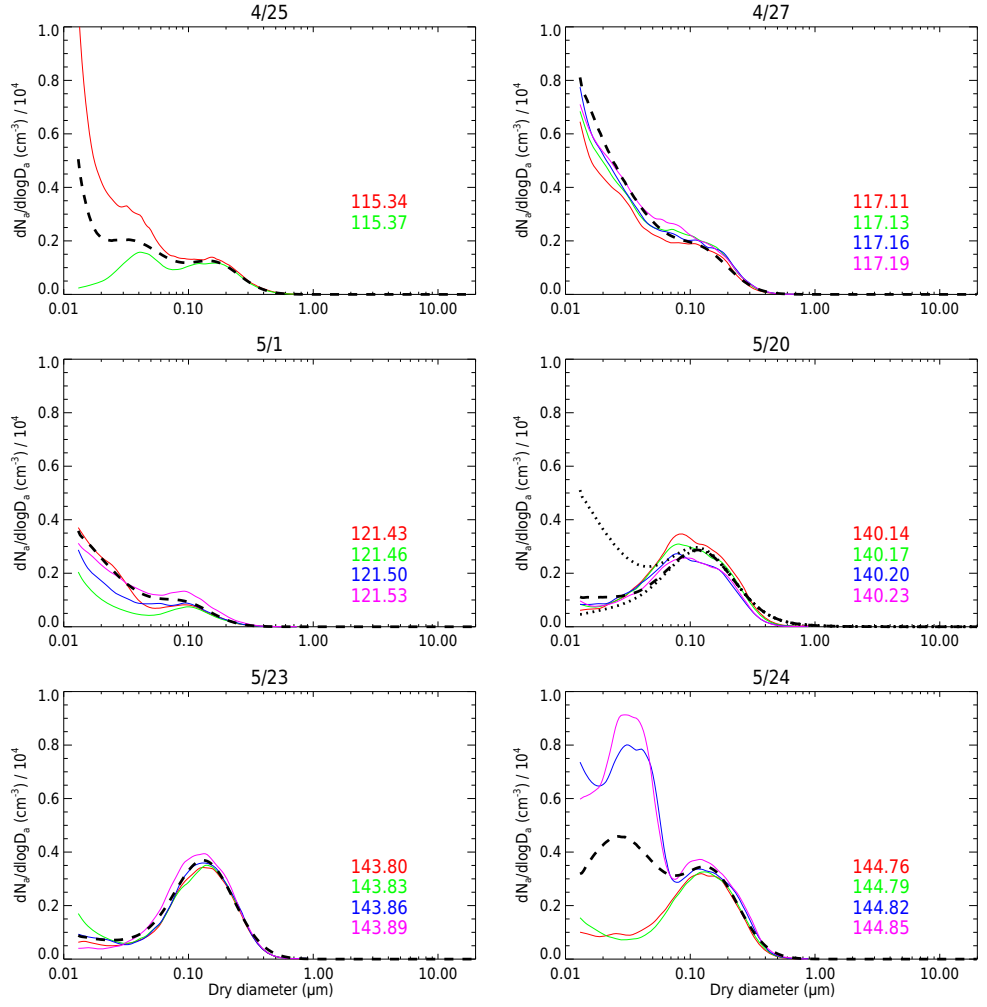

Figure 6. Aerosol dry number size distributions reported from HTDMA during the 2 h pre-rain period (colored solid lines; legend indicates Julian date in UTC) and the mean size distribution derived for each case study (black dashed lines; archived with Supplement 1). In the 20 May case, 0 and 8000 cm^{-3} particles in the nucleation mode illustrate the baseline (BASE) and sensitivity test (NUCL) simulation inputs (dotted black lines).

two modes provide a best fit, if the geometric mean diameter of the smaller mode is smaller than or equal to 0.01 µm, that mode is considered the smallest of three; otherwise, that mode is considered the middle of three. A simple linear average of the modal properties (number concentration, geometric mean diameter, and standard deviation) is then adopted in each of the three modes. A hygroscopicity parameter (κ) is then derived for each mode as follows. First, a κ value is calculated from the mean growth factor measured by the HTDMA during each pre-convective period, available in six size cuts over 0.013–0.40 µm in dry diameter. Then, a κ value is assigned to each HTDMA size bin using linear interpolation. Finally, a κ value is calculated for each mode as a number-weighted average over occupied bins.

3.4.2 Above 1 km

The number concentration in each mode is assumed to vary with height above the surface layer, and its variation is derived from aircraft measurements as follows. First, we adopt the ground-based three-mode fit for each case study as representative of the bottom kilometer of the atmosphere. Owing to an absence of fine-mode aerosol size distribution information aloft, we then assume that aerosol in the smallest mode is confined to the surface layer, consistent with the occurrence of increased concentrations primarily near the surface (Fig. 4). Numbers in the larger two modes above the surface layer are then determined as follows.

When only UHSAS data are available (first three case studies; see Fig. 4), in each 1 km layer above the surface layer, the number concentration in the larger mode is set to the total concentration measured by UHSAS, and the number concentration in the smaller mode is set such that the ratio of UHSAS to total assumed aerosol matches the experiment-wide median ratio at that altitude. Number concentrations in any of the smallest few UHSAS bins that exceeded 5 times the concentration in bins with diameter larger than 0.1 µm (in terms of $\mathrm{d}N/\mathrm{dlog}\,D$) appeared spurious, and these are neglected when present (e.g., as in lowest two levels in Fig. 7). The resulting number-wise scaling of the ground-based size distributions to the total UHSAS numbers obtained by aircraft often gives remarkably close fits to the UHSAS size distributions, as demonstrated in Fig. 7. However, nearest to the surface, aircraft measurements appear to be variably biased relative to the ground-based measurements: they are substantially biased low on 25 April, but perhaps not significantly, owing to very small sample size (see Fig. 7) versus modestly high on 27 April and close agreement on 1 May (not shown).

When only airborne CPC data are available (the second three case studies), then in each 1 km layer above the surface layer, the ratio of the number concentration of the larger aerosol mode to the smaller aerosol mode is set to the experiment-wide median as a function of height, and the total of both modes is set to the median concentration measured by airborne CPC in the corresponding 1 km layers.

Table 1. Summary of NASA Unified Weather Research and Forecasting (NU-WRF) simulations without and with aerosol input profile and prognostic droplet number concentration (N_d).

Experiment	Prognostic N_d	Nucleation-mode aerosol	Homogeneous freezing only
BASE	–	–	–
AERO	✓	–	–
NUCL	✓	✓	–
HOMF	✓	–	✓

For all case studies, at elevations above the aircraft measurements (5–10 km; see Fig. 4), the aerosol is fixed to that in the highest layer for which measurements are available. Resulting aerosol specifications for simulations of each case are archived as Supplement 1.

Owing to the relatively simple modal structure of the input aerosol profiles derived here, an estimated coarse mode could be appended using climatological data or other field measurements (e.g., Corr et al., 2016), but we do not attempt that here.

4 Evaluation of hydrometeor size distributions in 20 May case study simulations

4.1 Simulations

We demonstrate use of derived aerosol input data in the 20 May case study. Our simulations of the case (Table 1) use the NASA Unified Weather Research and Forecasting (NU-WRF) model (Peters-Lidard et al., 2015), set up as described by Tao et al. (2016), with an innermost domain of 1 km horizontal grid spacing (Tao et al., 2016, their Fig. 2). We compare observed hydrometeor size distribution properties with those simulated using Morrison et al. (2009) two-moment microphysics with hail. Except in one sensitivity test described below, we use all ice formation parameterizations that are standard in the NU-WRF implementation. Heterogeneous freezing of cloud droplets and raindrops is limited to temperatures colder than −4 °C. Immersion freezing of cloud droplets and raindrops follows Bigg (1953). Contact nuclei available to freeze cloud droplets are calculated as a function of supercooling following Meyers et al. (1992). Deposition and condensation freezing follows Thompson et al. (2004, their Eq. 2) in adopting the Cooper (1986, their Fig. 4.3) fit to ice concentrations measured in moderately supercooled clouds, except implemented where ice supersaturation exceeds 8 % or where liquid saturation is exceeded and temperature is colder than −8 °C; when those conditions are met, the number of cloud ice crystals nucleated is also not permitted to drive the total ice number concentration (including cloud ice, snow, and hail) over $500\,\mathrm{L}^{-1}$. All of these heterogeneous ice-nucleation parameterizations neglect spatial

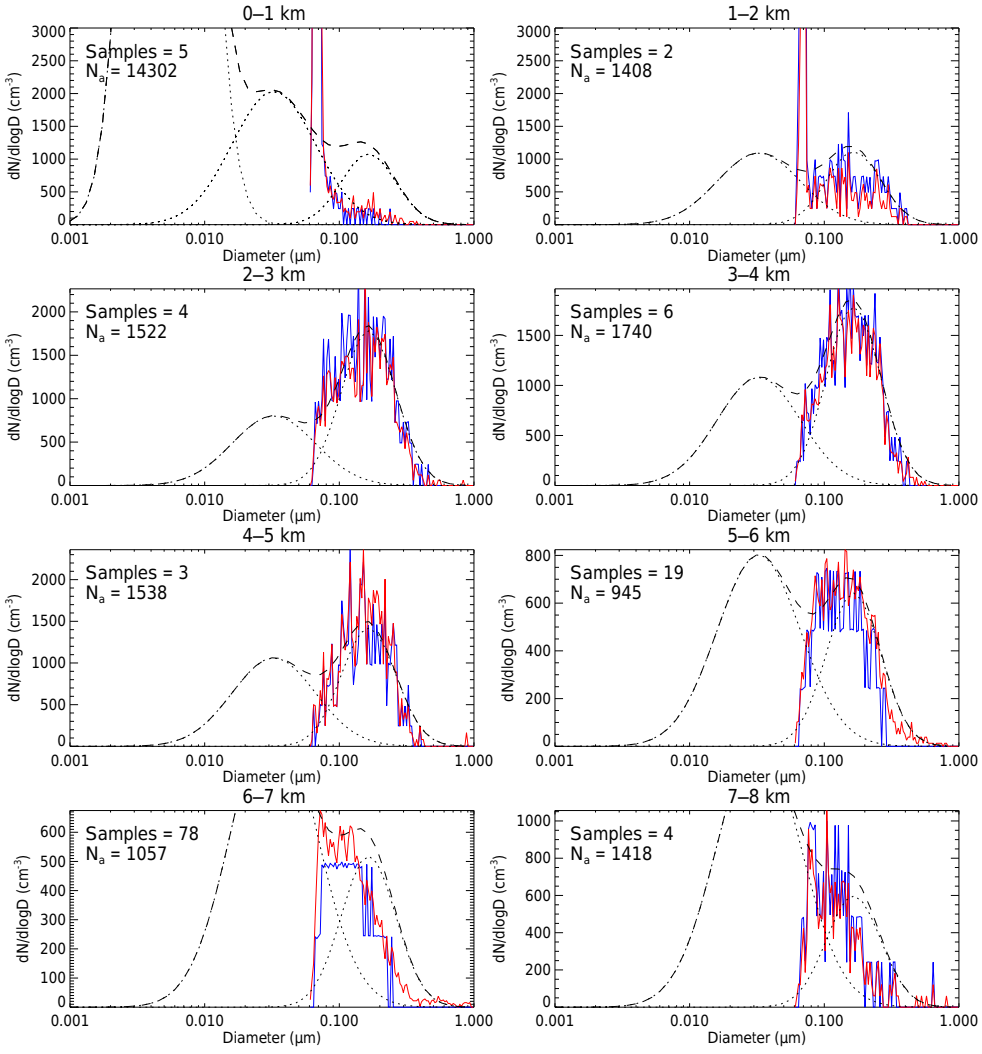

Figure 7. Derived modes and aerosol number size distribution over 1 km deep layers (black dotted and dashed lines, respectively) compared with bin-wise mean and median out-of-cloud UHSAS size distributions (red and blue lines, respectively) for the 25 April case study, with sample size (see Fig. 4) and total aerosol number concentration (N_a) in cm^{-3}.

variability and consumption of ice-nucleating particles. Secondary ice formation via rime splintering between −3 and −8 °C follows Hallett and Mossop (1974). Homogeneous freezing of cloud droplets and raindrops is instantaneous at −40 °C. A maximum cloud ice number concentration of $300\,L^{-1}$ is also imposed. Cloud ice number concentrations consistently exhibit $\sim 300\,L^{-1}$ maxima in all simulations reported here, but we found stratiform outflow size distributions compared with observations (see Sect. 4.2) were insensitive to removing that limit.

In the baseline simulation (BASE), we use a fixed droplet number concentration of $250\,cm^{-3}$. In the AERO simulation, droplet number concentration is treated prognostically as follows. Aerosol is initialized within all domains to the aerosol input profile derived as described in Sect. 3.4 (see Supplement 1), and is fixed to it at the outermost domain boundaries. Aerosol activation follows the treatment of Abdul-Razzak and Ghan (2000), in which the supersaturation is taken as the minimum value over the time step following Morrison and Grabowski (2008, their Eq. A10), as in Vogelmann et al. (2015, see their Sect. 5.1). This approach implemented in NU-WRF permits secondary activation of droplets above cloud base, as in Yang et al. (2015). During simulation time, aerosol is treated semi-prognostically as the sum of unactivated aerosol and droplets present, consumed by droplet collision–coalescence, and transported as in Fridlind et al. (2012, their "DHARMA-2M" simulation) and Endo et al. (2015, their "DHARMA BIN" simulations). Aerosol source terms beyond advection across outer domain boundaries are neglected (e.g., primary emission and gas-to-particle conversion). The HOMF simulation is identical to the AERO simulation except that all ice-nucleation and multiplication mech-

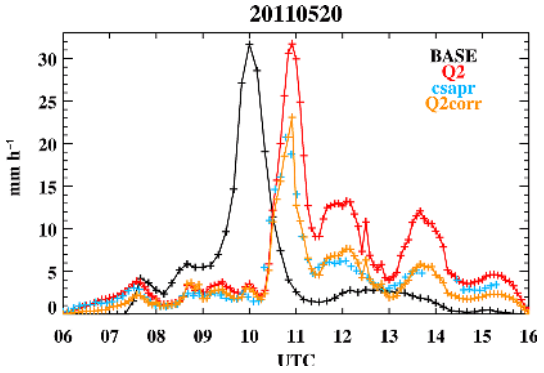

Figure 8. Time series of precipitation from the BASE simulation, National Mosaic and Multi-Sensor Quantitative Precipitation Estimate (Q2), C-SAPR, and gauge-corrected Q2 averaged over the region sampled by aircraft ∼ 13:54–14:54 UTC indicated by a red rectangle in Fig. 9.

anisms are turned off except for homogeneous freezing of cloud droplets and raindrops (see Table 1).

Since nucleation-mode aerosol (in the smallest fitted mode) is present very non-uniformly in time and space during some MC3E case studies (see Fig. 6), we finally test whether that is likely to be important. In a sensitivity test simulation (NUCL), 8000 cm^{-3} nucleation-mode particles are added to the bottom 2 km in a mode with geometric mean diameter of 0.005 µm and geometric standard deviation of 3. Based on the April and 1 May nucleation-mode fits listed in Fig. 6, this represents the most commonly fit mode diameter and mode standard deviation, and a modest number concentration (maximum on 1 May) that is lower than typically observed in the 10–30 nm diameter range during intense new particle formation events (e.g., Crippa and Pryor, 2013). To clarify the contrast between NUCL and AERO simulations, the nucleation-mode number actually fitted in the 20 May case is set to zero in AERO (dotted lines in Fig. 6). During the course of this study, minor changes were made to aerosol observation processing concurrently with the simulations being run; simulations therefore used a preliminary version of the 20 May aerosol input data that is negligibly different from the final version for our purposes. AERO and NUCL aerosol input files are included in Supplement 1 for completeness.

Over a 100 × 100 km domain centered on the C-SAPR radar, Fig. 8 shows the time series of surface precipitation derived from C-SAPR, from the National Mosaic and Multi-Sensor Quantitative Precipitation Estimate (Q2; Zhang et al., 2011) with and without rain gauge correction (Tang et al., 2014), and from the BASE simulation in the region sampled by the *Citation* aircraft (region bounded by the red rectangle in Fig. 9). The simulated squall line passes roughly an hour earlier than observed, which could be attributable to two general causes: (i) uncertainties in the initial and boundary conditions, including those influential to surface heat fluxes, and (ii) errors in model parameterization components, including microphysics scheme elements, which can independently influence the rainfall structure in NU-WRF simulations in this case (see Tao et al., 2016, their Fig. 11). Nonetheless, we find relatively good agreement between predicted and retrieved maximum precipitation rates (about 20–30 mm h^{-1}) and the duration of rates greater than 50 % of maximum (about 1 h). At a time representative of *Citation* aircraft sampling of the stratiform outflow (13:40 UTC), Fig. 9 shows a map of Q2 precipitation over the inner domain; the region sampled by the *Citation* aircraft is bounded by a red rectangle. Also shown is surface precipitation from the BASE simulation at the time of heavy stratiform precipitation (13:00 UTC; see Fig. 8). The BASE simulation shows a precipitation structure oriented in a band from southwest to northeast, similar morphologically to that observed, as do all sensitivity tests discussed below (not shown).

4.2 Comparison with in situ observations

4.2.1 Baseline simulation

As noted above, the 20 May case is unique during MC3E, owing to robust in situ sampling of extensive stratiform outflow from deep convection by the *Citation* aircraft (Wang et al., 2015a; Wu and McFarquhar, 2016). Here, we use ice number and mass size distributions derived from a Particle Measuring Systems (PMS) two-dimensional cloud (2DC) probe and a SPEC Inc. high-volume precipitation spectrometer (HVPS) probe (Baumgardner et al., 2011, and references therein) on the aircraft. Since the derivation of number and mass size distributions and their integrals from such probes introduces substantial sources of uncertainty that are often not well quantified to date (e.g., Baumgardner et al., 2011), we use two independent derivations described in Wang et al. (2015a) and Wu and McFarquhar (2016), which differ in details of the methods used to process and estimate mass from the raw image probe data. For computation of mass median area-equivalent diameter (MMD_{eq}), we follow the Wu and McFarquhar (2016) approach for a first estimate, substituting the Baker and Lawson (2006) habit-independent mass-area dimensional relation for a second estimate (Table 2).

Over the red-enclosed regions shown in Fig. 9, which bound the aircraft in situ sampling of stratiform conditions, Fig. 10 shows ice water content (IWC) and ice number concentration (N_i) from both independently derived observational data sets alongside simulated values. Observed ice number concentrations at three well-sampled elevations (Table 2) are within the range of those reported from nine storms measured over Colorado and Oklahoma in May and June 2012 during the Deep Convective Clouds and Chemistry Experiment (Corr et al., 2016, 10–120 L^{-1}). We have omitted analysis of observations at lower elevations (temperatures warmer than −10 °C), owing to initially suspected encounters with supercooled water, which can be difficult to confidently rule out (Wang et al., 2015a). Conditions at or near

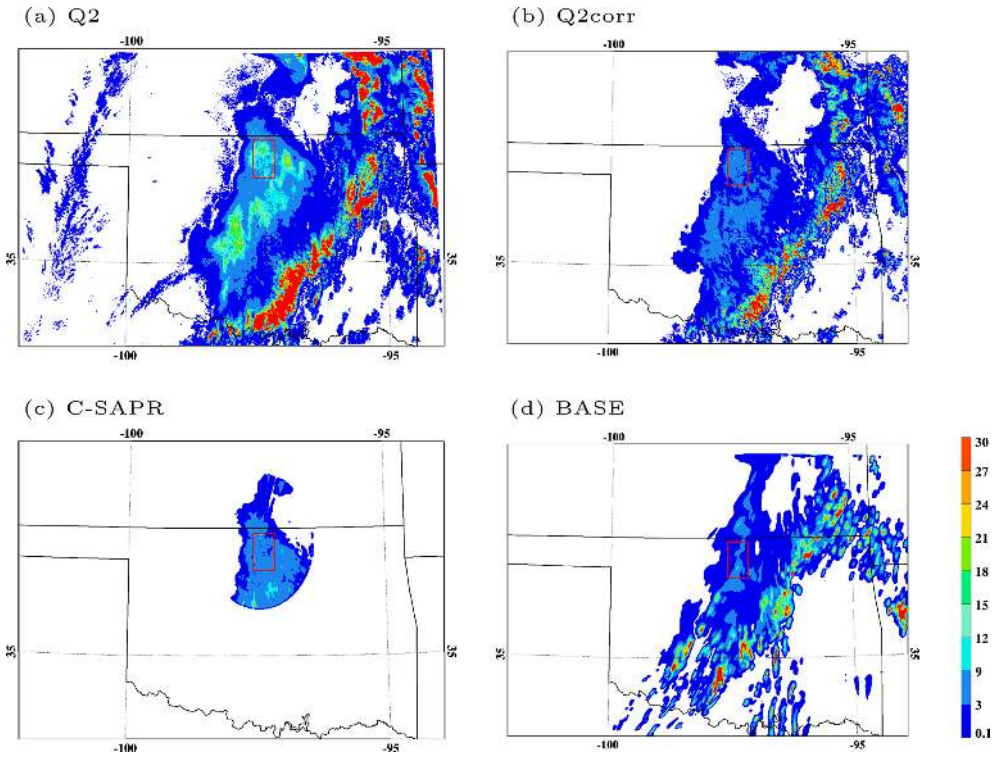

Figure 9. Surface precipitation rate (mm h^{-1}) from Q2 at 14:00 UTC **(a)**, gauge-corrected Q2 (**b**; see text) from C-SAPR at 13:40 UTC **(c)**, and in the BASE simulation at 13:00 UTC **(d)**. Red rectangles bound the *Citation* aircraft flight legs examined here.

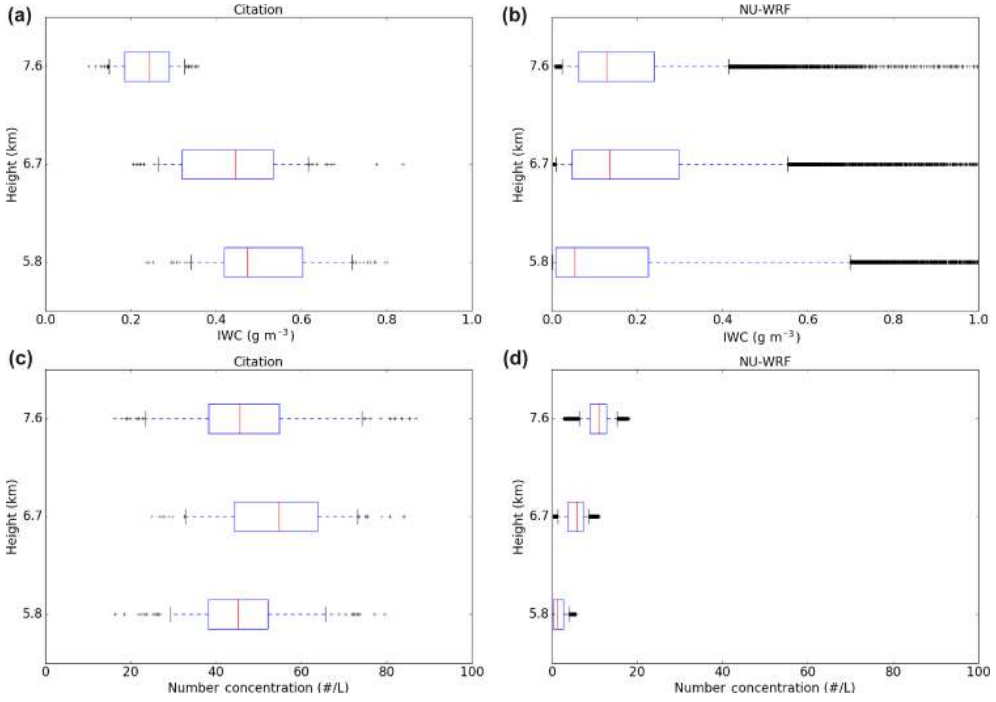

Figure 10. Total ice water content (IWC; **a**, **b**) and ice number concentration (N_i; **c**, **d**) derived from aircraft observations (**a**, **c**; see text) and from the BASE simulation **(b, d)** within the respective red-bounded geographic regions shown in Fig. 9. Simulated ice is the sum of all ice classes. Observed ice is the sum of all size bins shown in Fig. 11. Box and whisker symbols represent the median, inner half, and 5th and 95th percentiles.

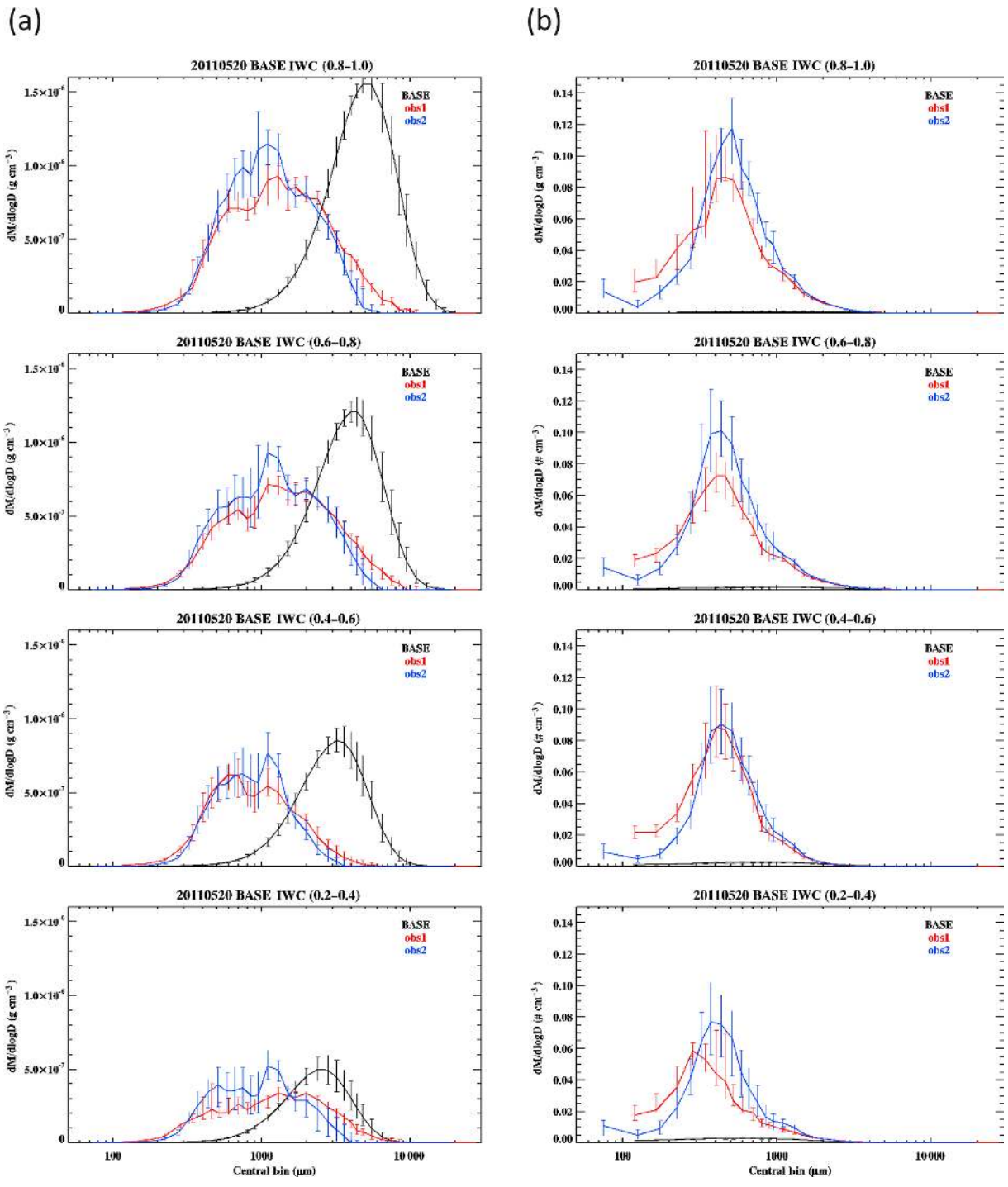

Figure 11. Size distributions of ice mass **(a)** and number **(b)** in four ranges of ice water content (IWC; ranges in parentheses in $g\,m^{-3}$) derived from the merger of two-dimensional cloud (2DC) and high-volume precipitation spectrometer (HVPS) raw data independently by Wang et al. (2015a, "obs1" in red) and Wu and McFarquhar (2016, "obs2" in blue). Both are shown as an estimate of poorly established uncertainty. Also shown are size distributions from the BASE simulation (black) at 5.8 km (−11 °C) within the respective red-bounded geographic regions shown in Fig. 9. Simulated ice is the sum of all ice classes at each size. The simulated ice bin size is the sphere diameter calculated from the bulk density of each ice class. The measured ice size is the randomly oriented maximum dimension. Error bars indicate 1 standard deviation of values simulated or observed at each size.

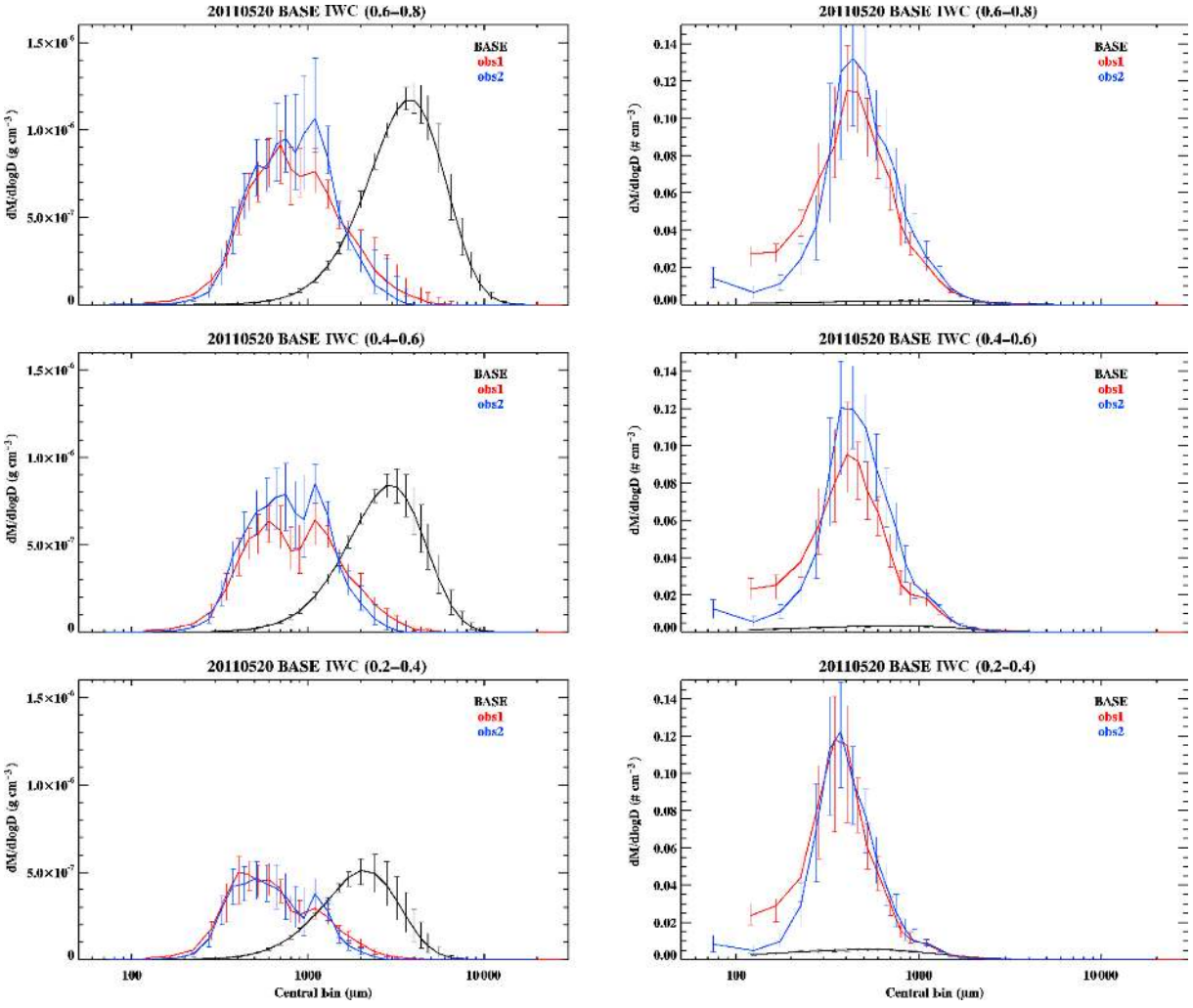

Figure 12. The same as Fig. 11 except at 6.7 km (−16 °C). No IWC greater than 0.8 g m^{-3} was measured at 6.7 km.

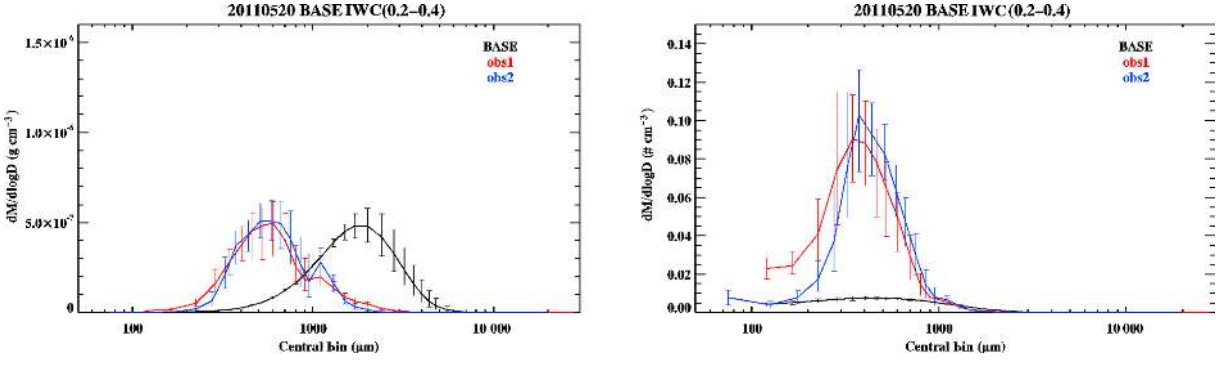

Figure 13. The same as Fig. 11 except at 7.6 km (−23 °C). No IWC greater than 0.4 g m^{-3} was measured at 7.6 km.

ice saturation are generally expected over heavy stratiform rain (e.g., Grim et al., 2009), but conditions ranging from liquid saturation to ice subsaturation above the stratiform melting layer could be associated with differing midlevel inflow positions or embedded convective-scale perturbations (e.g., Barnes and Houze, 2016). Later analyses of the 20 May case provide evidence of local ice subsaturation above the melting level associated with bright band variability observed in C-SAPR fields (Kumjian et al., 2016). Here, we focus on the

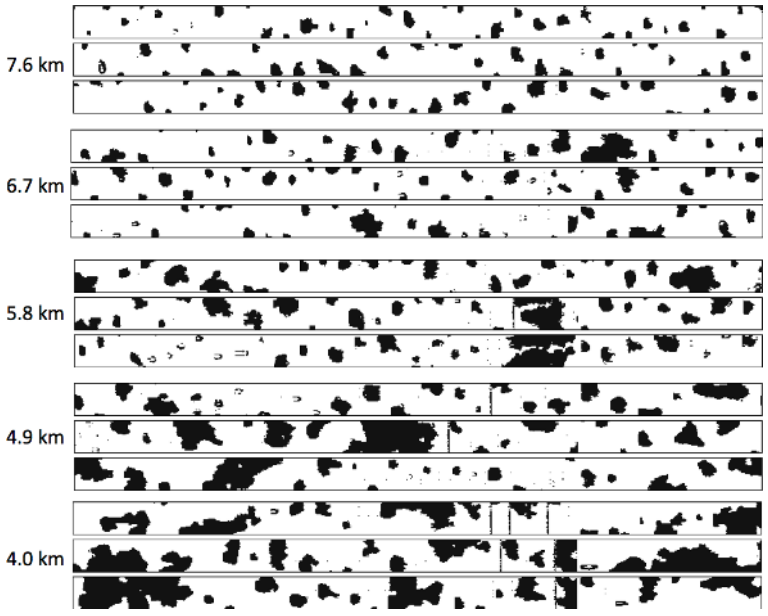

Figure 14. A 2DC image collage from flight legs above the melting level in the 20 May stratiform outflow region. Three time series examples are given at each elevation. The vertical dimension of each time series is 960 µm. Here, we focus on the top three elevations that are greater than ∼ 1 km above the variable melting level height of ∼ 3.9 km (see text).

Table 2. Aircraft-observed temperature (T), ice water content (IWC), ice crystal number concentration (N_i), and mass median area-equivalent diameter (MMD_{eq}) statistics by flight leg elevation, with the range given over two derivation methods (see text).

Elevation (km)	Median T (°C)	T range (°C)	Mean IWC (g m^{-3})	Max. IWC (g m^{-3})	Mean N_i (L^{-1})	Max. N_i (L^{-1})	Mean MMD_{eq} (µm)	Max. MMD_{eq} (µm)
7.6 km	−23	−22.4 to −23.0	0.21–0.28	0.38–0.43	39–47	78–87	515–530	900–1025
6.7 km	−16	−16.0 to −16.8	0.44–0.50	0.94–0.96	51–54	84–100	701–704	1025–1200
5.8 km	−11	−10.2 to −11.7	0.52–0.56	0.89–1.0	45–46	72–80	948–993	1850–2200

top three elevations that were well sampled and consistently more than 1 km above the variable bright band zone.

The aircraft observations shown in Table 2 are taken from five level legs flown between 13:54 and 14:54 UTC, except roughly one-third of the observations at −23 °C that are taken from an isolated level leg later in the same flight (see Wang et al., 2015a, their Fig. 5). Since results are not sensitive to excluding the later samples, we consider the observations statistically representative of the 13:54–14:54 UTC time period. For our comparisons, simulations are sampled roughly 1 h earlier, consistent with earlier squall line passage, using 10 min output fields between 13:00 and 14:00 UTC.

With increasing elevation in the BASE run, summing all model ice classes, simulated IWC generally decreases while N_i increases; both observational analyses show similar patterns in some respects, although the trend in N_i across the three best sampled elevations is not discernible. Overall, the largest apparent deviation of simulations from observations in Fig. 10 is roughly 4–10 times fewer ice crystals, although sampling remains relatively sparse and observational uncertainty could be very large. We do not attempt to quantify uncertainty in N_i here, owing to the difficulty of doing so and the relative lack of importance to analyses below, which are primarily focused on the size distributions of mass rather than number. In similar simulations of the 20 May case, Fan et al. (2015) show a similar order of magnitude underestimation of measured N_i.

Figures 11–13 show the underlying mass and number size distributions at the three well-sampled elevations (5.8, 6.7, and 7.6 km) as a function of ice crystal randomly oriented maximum dimension (D_{max}; see Wu and McFarquhar, 2016). At 5.8 km (−11 °C), simulated and observed mass and number size distributions are compared in four mass concentration intervals spanning 0.2–1 g m^{-3} (Fig. 11). Consistent with underpredicted N_i, the D_{max} at which BASE mass distributions peak is roughly 3–5 times larger than that at which the observed size distributions peak. The D_{max} at which the BASE mass distributions peak increases monotonically with increasing mass, whereas the observed mass size distributions tend to peak consistently at D_{max} of roughly 1–2 mm,

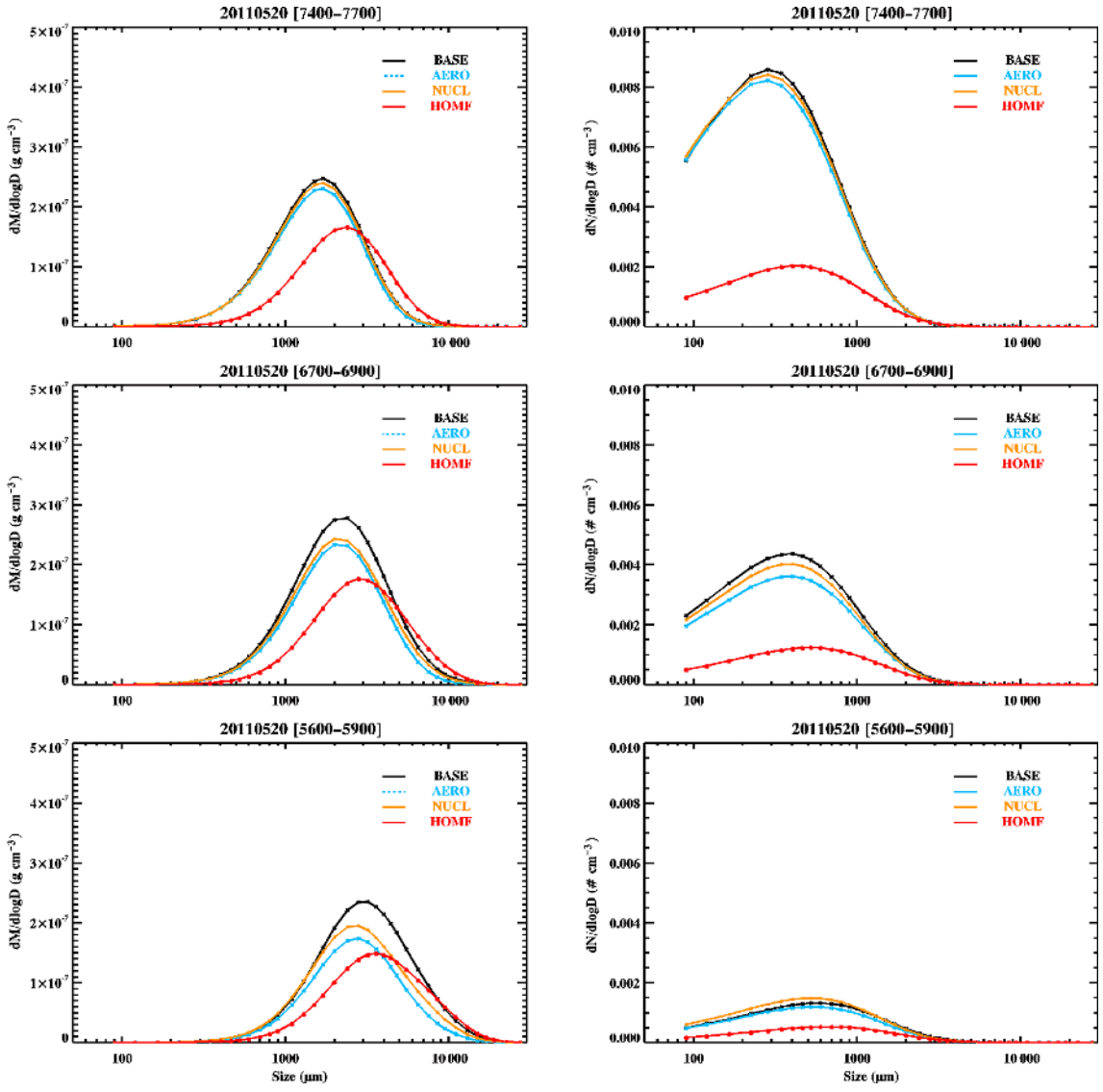

Figure 15. Simulated ice number and mass size distributions averaged over the red-bounded geographic region shown in Fig. 9 at 13:00–14:00 UTC. Each panel shows the results from four simulations as labeled (cf. Table 1).

generally independent of IWC range; other recent deep convection observations have found notably weak dependence of convective outflow ice size on mass concentration at fixed elevations (Fridlind et al., 2015; Leroy et al., 2015). We note that the $D_{\max}$, at which observed and simulated size distribution lines cross one another, is greater for number than for mass because the effective density of the relevant ice particles (namely, snow) is less in the observations than in the model microphysics scheme (0.1 g cm^{-3}; Morrison et al., 2009). Overall, there is a marked absence of particles with $D_{\max} < 1000\,\mu$m in the BASE simulation, suggesting that they are not produced or are lost via a process such as aggregation.

Observed number size distributions peak at $D_{\max}$ of roughly 400 μm, which does not significantly change with either mass mixing ratio or elevation (see Figs. 12–13). At 6.7 and 7.6 km (−16 and −23 °C), however, mass size distributions appear to fall into two modes: one peaking at $D_{\max} \sim 500\,\mu$m (most apparent at the lowest mass mixing ratios) and a second peaking at $D_{\max} \sim 1$ mm. The $D_{\max}$ where observed number size distributions peak (at all elevations and mass concentrations) is similar to that where the smaller-mode mass size distribution peaks. In the observations, evolution with decreasing height from alignment to non-alignment of the mass and number size distribution peaks (namely, a shift of the mass size distribution peak to larger sizes that is not accompanied by a shift of the number size distribution peak) is suggestive of aggregation that is adequate to increase mass median $D_{\max}$ but insufficient to

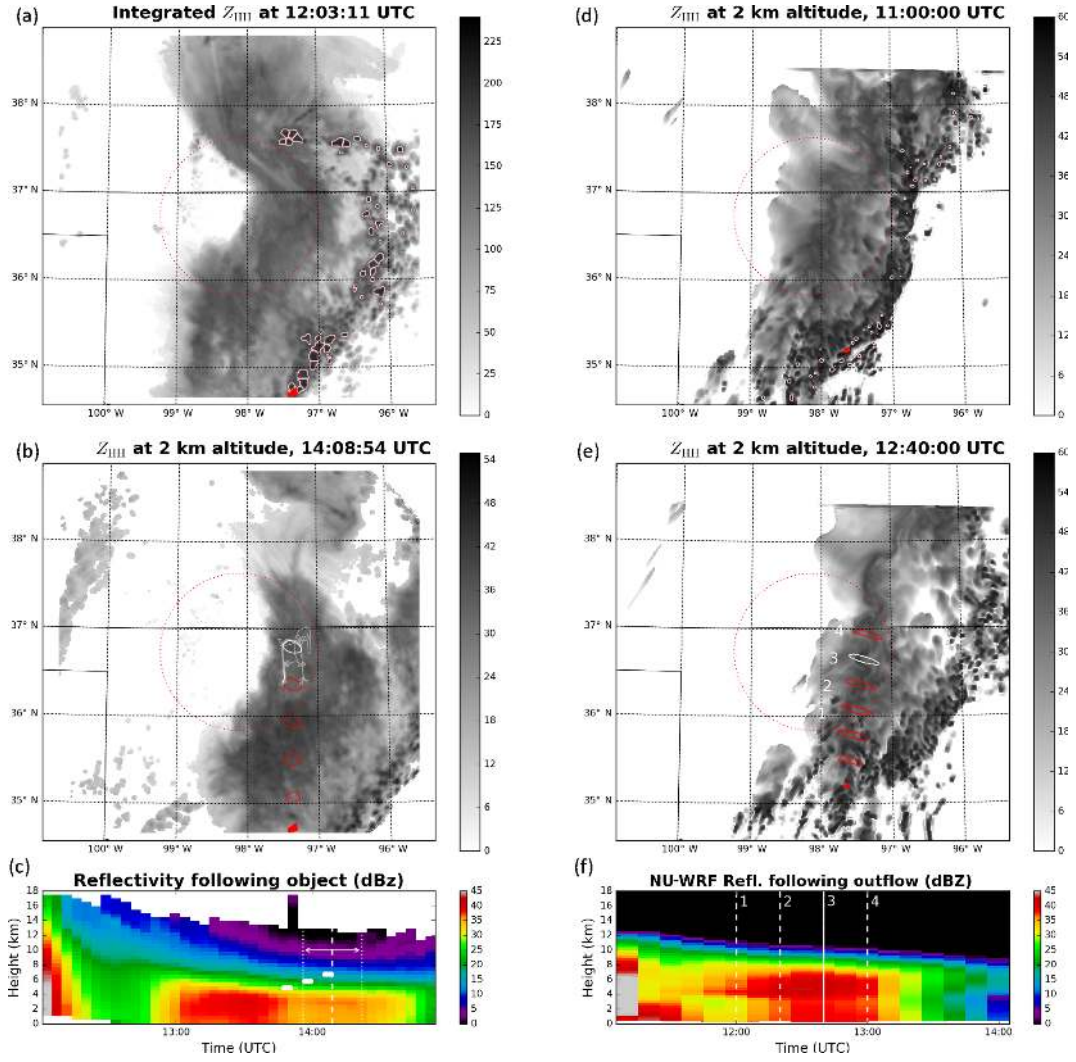

Figure 16. Horizontally polarized radar reflectivity (Z_{HH} in dBZ) from KVNX radar (dotted red circle): **(a)** example updraft object at ∼ 12:00 UTC (solid red) among others identified in units of dBZ kilometers (red enclosed; see text); **(b)** movement of example updraft from initial location (solid red) towards intersection with the aircraft sampling location (white enclosed; see text) projected onto 2 km Z_{HH} at ∼ 14:00 UTC; and **(c)** Z_{HH} curtain obtained from column-wise averages over tracked regions from ∼ 12:00 to 15:00 UTC with *Citation* ascent legs in time and height (white bars) and averaging time used in Fig. 17 (white lines). From the AERO simulation: **(d)** identification of a typical updraft object projected onto simulated Z_{HH} at ∼ 11:00 UTC (solid red) among others identified (red enclosed; see text); **(e)** its movement from the identified location (solid red) to the intersection with the aircraft sampling location (white enclosed; see text) projected onto simulated 2 km Z_{HH} at ∼ 13:00 UTC; and **(f)** Z_{HH} curtain obtained from column-wise averages over tracked regions from ∼ 11:00 to 14:00 UTC with the midpoint of hour-long averages used in Fig. 17 (white lines).

increase number median D_{max}, conceivably, owing in part to greater sticking efficiency among larger colliding particles.

Subjective inspection of ice crystal images generally shows that aggregates are more common at larger sizes and lower elevations, consistent with the possibility that aggregation may be largely responsible for the coherent trend in observed particle size with elevation. However, the general irregularity of the ice particles (Fig. 14) makes confidently distinguishing aggregates from non-aggregates far more difficult than in a case where dendrites are the dominant habit, for instance, and aggregate fraction can be readily estimated for simulation evaluation (e.g., Avramov et al., 2011). In this case, aggregates appear present at the highest elevation sampled (−23 °C), but it has been suggested that aggregation may be a negligible process at temperatures warmer than −20 °C (e.g., Barnes and Houze, 2016) and we cannot rule out the possibility that aggregation is not a dominant determinant of size distribution trends seen here in observations between −10 and −23 °C.

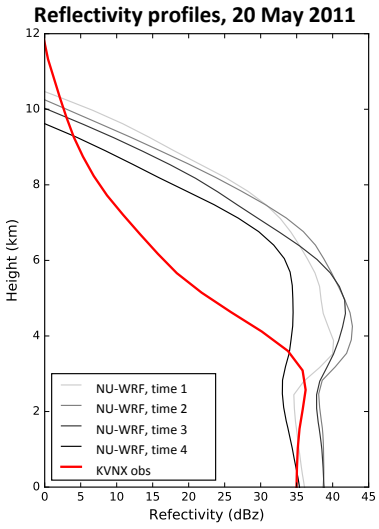

Figure 17. Reflectivity profiles obtained from the 1 h average of reflectivity time series shown in Fig. 16 from KVNX (red line) and AERO simulation times 1, 2, 3, and 4 indicated in Fig. 16 (light to dark grey lines).

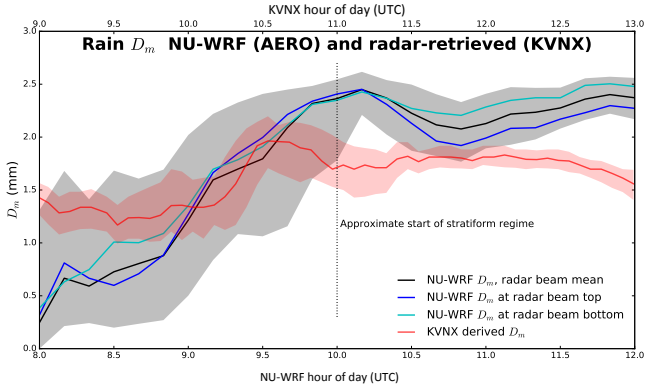

Figure 18. Mass-weighted mean diameter (D_m) as a function of time in the AERO simulation and in retrievals averaged over the respective red-bounded geographic regions shown in Fig. 9. Lines indicate median values (see legend). Shaded regions indicate the inner half of retrieved values and simulated values at the radar beam mean height. Note the offset in time axes (top and bottom) to align approximate timing in observations versus simulations.

4.2.2 Sensitivity tests

Figure 15 demonstrates the effect of replacing fixed droplet number concentration in the BASE simulation with the aerosol input data derived in Sect. 3 and prognostic droplet number concentration. The AERO ice size distributions are found to be largely unaffected compared with the BASE simulation. If nucleation-mode aerosols are added to the aerosol input file (NUCL simulation), results are similarly little affected. Inner-domain averages of cloud water mixing ratio and number concentration indicate that AERO droplet number concentrations are substantially smaller than fixed BASE values, especially aloft, and nucleation-mode aerosols are scarcely activated in the NUCL simulation (not shown). A sensitivity test in which all heterogeneous freezing parameterizations and ice multiplication mechanisms are turned off (HOMF), by contrast, results in substantially larger and fewer outflow ice crystals, worsening agreement with observations (see Fig. 15). Whereas favoring homogeneous freezing of droplets generally yields more ice particles in an updraft parcel (e.g., DeMott et al., 1998), here we find the opposite in aged stratiform outflow, where snow is the dominant hydrometeor class. Snow number concentration maxima intermittently reach $\sim 500\,\mathrm{L}^{-1}$ in all simulations except HOMF, where they reach only $\sim 30\,\mathrm{L}^{-1}$. Since $500\,\mathrm{L}^{-1}$ is the limit imposed on the Cooper (1986) parameterization contributions to total ice number concentration (see Sect. 4.1), we conclude that removing that source is likely chiefly responsible for larger ice in HOMF outflow. We note that species number concentrations are not conserved by design in order to enforce limits on size distribution slope parameters (Morrison et al., 2009), which complicates drawing firm conclusions about the contributions of specific processes. In summary, we find that the combined effects of heterogeneous ice nucleation and ice multiplication have a greater effect on outflow ice size than droplet spectra changes over the range in BASE versus AERO simulations. The fact that all of the simulations also substantially overestimate outflow ice size (where directly observed) is consistent with the possibility that the microphysics scheme could be missing some critical aspects of ice nucleation or ice multiplication.

In all simulations, N_i decreases by roughly a factor of 8 between 7.6 and 5.8 km (as in Fig. 10). Observed N_i does not show a discernible trend over the well-sampled elevations examined here (Table 2). These results suggest that simulated aggregation is more aggressive than observed in this case. In Fan et al. (2015) simulations of the same case with another two-moment scheme and a size-resolved microphysics scheme, N_i decreases by roughly a factor of 20 over a similar altitude range (see their Fig. 11b). Profiles of stratiform N_i measured during the Bow Echo and Mesoscale Convective Vortex Experiment (BAMEX) exhibited a 25 % decline per degrees Celcius between 0 and −10 °C, but were not reported at colder temperatures (McFarquhar et al., 2007; Smith et al., 2009). Because measurement uncertainty in N_i remains essentially unquantified to date (e.g., Fridlind et al., 2007, uncertainty estimated at a factor of 5), we do not attempt to draw conclusions at this point.

4.3 Comparison with radar observations

4.3.1 Radar reflectivity

Radar reflectivity time series from the National Weather Service Next-Generation Radar (NEXRAD) network Weather Surveillance Radar-1988 Doppler (WSR-88D) radar located

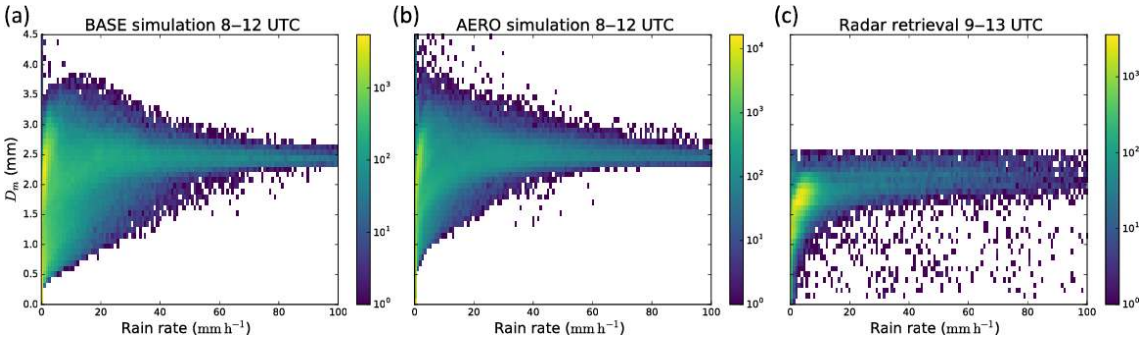

Figure 19. Joint histogram of mass-weighted mean diameter (D_m) and collocated precipitation rate in BASE and AERO simulations and retrievals averaged over the red-bounded geographic region shown in Fig. 9 at 08:00–12:00 UTC (simulated) or 09:00–13:00 UTC (retrieved).

at Vance Air Force Base (KVNX) can place the aircraft-sampled elevations and locations into greater context. By identifying columns of enhanced specific differential phase above the melting level in KVNX data, which can be taken as an indication of updraft location (van Lier-Walqui et al., 2016a), and using the nearest radiosonde to represent horizontal winds, we estimate that roughly 2 h passed between ice detrainment from updrafts at roughly 35.5° N and *Citation* sampling at roughly 36.5° N (Fig. 16, left panels). A similar analysis of supercooled liquid water above the melting level and horizontal winds in the BASE simulation indicates a slightly shorter time period (Fig. 16, right panels); we have not attempted to objectively optimize this analysis since results are not strongly sensitive to choice of time and location, owing to the fact that conditions are quite horizontally uniform in both observed and simulated stratiform outflow.

Figure 17, derived from the fields shown in Fig. 16, illustrates that simulated reflectivity profiles below roughly 9 km are biased high in the AERO simulation, but simulated reflectivity above roughly 10 km is biased low. Thus, specifically at the elevations where the aircraft sampled (Fig. 16, white bars in observed reflectivity), simulated reflectivity is substantially greater than observed, consistent with ice particles substantially larger than observed (Figs. 11–13), but that is not the case at all elevations. Referring back to Fig. 16 (bottom panels), it is apparent that ice detrained from updraft tops in the AERO simulation may be either insufficiently concentrated or too small, but we have no direct measurements to confirm either possibility. At 8 km, Fan et al. (2015) simulations using both two-moment and size-resolved microphysics schemes show similar significant overestimations of reflectivity within stratiform outflow (see their Fig. 3b), indicative of similar biases in ice size (systematically larger than observed).

4.3.2 Polarimetric retrievals

The radar fields used to place aircraft sampling into context are also sensitive to rain size distribution beneath the *Citation* sampling location. Figure 18 shows the median and inner half of raindrop mass-weighted mean diameter (D_m; the fourth moment of the drop number size distribution divided by the third moment) as retrieved from KVNX data following Ryzhkov et al. (2014), with an estimated uncertainty of roughly 5–10 % (Thurai et al., 2012). The retrievals shown are made along the lowest-elevation KVNX beam, which varies in height with distance, but simulated values vary relatively little over that height range for the subregion selected to match the *Citation* sampling location. In that stratiform region (rectangular regions in Fig. 9), at the onset of the heaviest stratiform precipitation (13:00 UTC observed, 12:00 UTC simulated; see Fig. 8), simulated median D_m is roughly 40 % (0.7 mm) larger than observed, consistent with simulated stratiform ice size larger than observed at 5.8 km (roughly 2 km above the melting level).

Retrieved D_m of 1.5–2 mm in the stratiform regime is on the high end of climatological values for various locations (Thurai et al., 2010, their Fig. 2), but quite similar to stratiform values measured by disdrometer and retrieved from profiling radar in the same storm (Williams, 2016, their Fig. 5b) and also in a tropical mesoscale convective system (Varble et al., 2014b, their Fig. 17). Simulated D_m values are larger than the upper end of stratiform values climatologically and show a high bias also found in similar simulations under tropical conditions using the same scheme (Varble et al., 2014b, "WRF-2M" in their Fig. 17).

Figure 19 shows simulated (BASE and AERO) and retrieved D_m values as a function of collocated precipitation rate. Simulated stratiform rain D_m values shown in Fig. 18 (selected to match the *Citation* location during aircraft sampling) are roughly equal to the microphysics scheme's breakup equilibrium value of 2.4 mm (Morrison and Milbrandt, 2015), which is seen throughout the high-precipitation rate limit in simulations. Observed D_m asymptotes more monotonically to a relatively broader range in the high-precipitation rate limit, where many retrieved values lie within retrieval uncertainty of 2.4 mm. We note that breakup equilibrium is thought to require rain rates on the order of 50 mm h^{-1}, substantially greater than typical of stratiform

conditions (e.g., less than 15 mm h^{-1} in Fig. 8), but its existence, size distribution characteristics, and prevalence in nature have been elusive (e.g., McFarquhar, 2010; D'Adderio et al., 2015).

We also note that a mass-weighted mean diameter of 2.4 mm corresponds to a mean volume diameter of 1.1 mm for an exponential size distribution in the microphysics literature (e.g., Morrison and Milbrandt, 2015, their Appendix C), whereas the two diameters with the definition of the latter are used interchangeably in the radar literature (e.g., Testud et al., 2001). Considering raindrop size in general terms, the reduced droplet number concentrations in the AERO versus BASE simulation are associated here with a reduction in the frequency of D_m values below 2.4 mm at convective rain rates of 20–40 µm (see Fig. 19). This reduction is consistent with a pattern of increasing raindrop size with increasing aerosol or droplet number concentration shown in past modeling studies over a wide range of thermodynamic conditions (e.g., Storer et al., 2010) and also found over multi-day statistics using similar retrievals of raindrop size alongside ground-based aerosol observations under tropical conditions (May et al., 2011).

5 Summary and discussion

We report hygroscopic aerosol size distribution profiles for six convection case studies observed during the MC3E field campaign over Oklahoma. Each profile is derived by merging ground- and aircraft-based measurements. Missing aircraft data, owing to instrument failures, are filled by using experiment-wide analysis of flights where all instruments functioned well. The aerosol profiles, archived as Supplement 1, are intended for use in modeling studies of convection microphysics, where both aerosol and hydrometeor size distribution data are required to evaluate fidelity of model physics.

We demonstrate use of the aerosol size distribution profiles in NU-WRF simulations of the 20 May case study, where widespread stratiform outflow was also well sampled by aircraft. Using Morrison et al. (2009) two-moment microphysics with hail in NU-WRF as an illustrative example, we compare simulated ice size distributions with measurements made in the outflow region. Across several sensitivity tests (Table 1), we find that both predicted and observed stratiform ice size distributions exhibit relatively well-defined properties that do not vary rapidly in time. However, simulated ice number concentrations (N_i) are roughly 5–10 times lesser than observed and the peak of ice mass size distributions roughly 3–5 times larger, correspondingly. Results are insensitive to prognosing droplet number concentration using an observation-based profile with or without nucleation-mode aerosol (which is found to be spatiotemporally variable across case studies). Additionally, turning off all ice-nucleation and multiplication parameterizations except homogeneous cloud droplet and raindrop freezing leads to less and larger ice.

Across three well-sampled elevations between 5 and 8 km (at −10, −17, and −23 °C), observed ice number size distributions peak at a randomly oriented maximum dimension (D_{max}) of roughly 400 µm at all elevations and lack a discernible vertical trend in total N_i (Table 1). At the highest elevation sampled, the derived mass size distribution appears to peak at a D_{max} only slightly larger than 400 µm. At lower elevations, the peak D_{max} of the observed mass size distribution is shifted to a size twice as large, at roughly 1 mm, perhaps owing to aggregation that is apparent in ice crystal images. However, some mass remains in the smaller size range where numbers are always concentrated. In simulations, unlike in observations, the D_{max} where the mass size distribution peaks increases substantially with mass concentration at each elevation (where there is more ice mass, it is also systematically larger) and the number concentration decreases rapidly with elevation. Beneath the aircraft-sampled region, simulated mass-weighted mean diameter of rain is roughly 0.7 mm larger than retrieved, consistent with overlying ice size bias; collocated reflectivity within the range observed is consistent with a corresponding low bias in precipitation rate (Fig. 8).

In general, stratiform microphysics features seen in this 20 May midlatitude squall line case appear notably similar to those observed in the tropics, as during the recent High Altitude Ice Crystals/High Ice Water Content (HAIC/HIWC) campaign that sought to robustly characterize ice properties that might be encountered by commercial aircraft transiting mesoscale convective systems around Darwin, Australia (Dezitter et al., 2013; Leroy et al., 2015, 2017). Perhaps most prominently, ice mass median area-equivalent diameter (MMD_{eq}) values of 500–700 µm between −15 and −25 °C (Table 2) are close to those found around Darwin in the same temperature range, and MMD_{eq} maxima of 900–1200 µm are also within the range found there (Leroy et al., 2017, their Figs. 6 and 9). Figures. 12 and 13, where the mass size distributions shown are visually integrable, show that the majority of mass in the 20 May case is generally found in a size range roughly bounded by half and twice the mass median size. Despite quite a bit of scatter, this condition found during HAIC/HIWC (Leroy et al., 2017, their Fig. 9) is indicative of a relatively narrow mode of ice mass around its median size, similar to that previously reported by Heymsfield (2003) from a combination of tropical and midlatitude measurements. We leave more detailed comparison of MC3E and HIWC/HAIC size distributions to future work but briefly note several other general similarities here.

Although we have not identified the capped column habit that is common among convective ice crystal habits in the tropics (e.g., Grandin et al., 2014; Ackerman et al., 2015), there is a predominance of irregular, compact crystals on 20 May (see Fig. 14), similar to those seen in tropical convective outflow during HAIC/HIWC (Leroy et al., 2015) and

during the Tropical Composition, Cloud and Climate Coupling and NASA African Monsoon Multidisciplinary Analyses field campaigns (Lawson et al., 2010). A less prominent similarity that can be generally gleaned from Figs. 11 and 12 is that the ice size distributions on 20 May show relatively weak correlation of ice mass median D_{max} with IWC at fixed elevations aloft, especially in contrast to simulations here; a similar observation–simulation contrast has been reported under tropical conditions (Ackerman et al., 2015, their Fig. 3). Over 10 °C temperature intervals colder than −5 °C (analogous to level flight legs here), HAIC/HIWC Darwin observations show a pattern of MMD_{eq} increasing or decreasing by less than 100–200 µm over a wider range of IWC sampled during HAIC/HIWC (up to $\sim 3\,g\,m^{-3}$ in Leroy et al., 2017) than sampled here (up to $1\,g\,m^{-3}$; Table 2). Profiles of Rayleigh reflectivity and Doppler velocity from a widespread tropical stratiform rain sampled during the Tropical Warm Pool-International Cloud Experiment (TWP-ICE) (Fridlind et al., 2015, their Fig. 11) also appear similar to the 20 May observations (Fig. 17; Doppler velocity not shown here), consistent with generally similar stratiform ice size distributions over tropical and 20 May conditions.

We speculate that similar updraft microphysical pathways that determine stratiform outflow ice properties are active in this 20 May case as in the tropical convection observed on many flights during HAIC/HIWC. This can be considered quite surprising since midlatitude continental convection updrafts are well known to be much stronger than their tropical oceanic counterparts (e.g., Liu and Zipser, 2015). However, it appears that deep convection updrafts may be direct source regions for individual outflow ice crystals (especially at upper elevations), consistent with the standard conceptual model of stratiform ice generation (e.g., Biggerstaff and Houze, 1991), and that ice which becomes stratiform rain may also exhibit rather narrow mass size distributions of relatively small crystals, consistent with an earlier and less complete data set gathered by Airbus (Grandin et al., 2014; Fridlind et al., 2015). The outflow ice size distributions, especially at lower elevations, are also modified at least in part by aggregation, consistent with layered patterns of ice crystal morphology obtained from dual-polarimetric radar particle identification within tropical stratiform precipitation decks (Barnes and Houze, 2016). However, contributions to the structure of aged anvil ice size from differences in detrained size with elevation are not clear at temperatures between approximately −10 and −20 °C in the 20 May case, where signatures of dendritic growth are absent but reflectivity and mean Doppler velocity are generally increasing towards the melting level. In other words, the relative roles of detrained size, differential sedimentation, and aggregation in shaping vertical trends in stratiform ice size distribution are not clear.

The aircraft engine issues that motivated the HAIC/HIWC campaign are thought to be associated with unexpectedly high IWC for given radar reflectivities (Lawson et al., 1998; Mason and Grzych, 2011; Leroy et al., 2015). Such conditions, which require mass concentrated relatively narrowly in relatively small ice crystals, have been documented at midlatitudes (Mason and Grzych, 2011). Whether or not they occurred in the 20 May case, it appears likely that a similar set of microphysical processes was active. Furthermore, it appears likely that such processes are not well represented in bin or bulk microphysics schemes generally (e.g., Ackerman et al., 2015; Fan et al., 2015; Varble et al., 2014b; Barnes and Houze, 2016). In one observation-driven modeling study, for instance, Zeng et al. (2011) propose an ad hoc "ice enhancement factor in the tropics" to bring simulations into statistical agreement with space-borne radar measurements. Developing tropical cumulus updrafts have also exhibited rapid ice production via ice multiplication that could depend on splinters formed during drop freezing rather than riming, which is not well understood to date and not represented in any commonly used microphysics scheme, and which may have a dominant impact on observed and simulated updraft glaciation rates (Lawson et al., 2015).

In parcel simulations designed to study how relatively narrow mass size distributions of substantial outflow ice could develop within tropical updrafts detraining at roughly −40 °C, Ackerman et al. (2015) concluded that copious crystal production at temperatures warmer than roughly −10 °C is required. In that study, copious mass concentrated in a relatively narrow size distribution centered on an area-equivalent diameter of ∼ 300 µm required an ice growth time period much longer than that available after homogeneous droplet freezing occurring less than ∼ 1 km lower. Given an updraft speed profile, increasing number concentrations of ice at temperatures of approximately −10 °C increased the IWC carried to −40 °C; any microphysical processes that competed with vapor growth of the ice crystals nucleated near −10 °C served to reduce the IWC available for detrainment at −40 °C. Conversely, an absence of ice production near −10 °C favored microphysical pathways that produced larger hydrometeors that sedimented from updrafts rather than detraining, consistent with simulations of tropical deep convection generally producing too little IWC over stratiform rain areas (e.g., Varble et al., 2014b).

Differences between the simulated 20 May stratiform ice microphysics and observations shown here could arise variously from differences between model and natural ice crystal physical properties (density or structure of crystals), their associated fall speeds, aggregation and vapor growth rates, and the coupling of processes within outflow-generating updrafts, in addition to the ice crystal production rates via primary nucleation and ice multiplication. The NU-WRF biases relative to observations shown here are consistent with the hypothesis that microphysics schemes are missing a key aspect of an updraft microphysics pathway that can largely determine outflow size, most likely associated with warm-temperature ice multiplication (e.g., Ackerman et al., 2015; Lawson et al., 2015; Ladino et al., 2017). Here, we show that

NU-WRF biases in stratiform ice mass size distribution are worsened when warm-temperature contributions to ice formation are decreased; Ackerman et al. (2015) find the same in parcel simulations and also demonstrate how biases can be decreased when warm-temperature contributions are substantially increased. In the simulations shown here, we also speculate that gravitational collection of stratiform ice may be too efficient, at least in the middle troposphere, as evidenced by reflectivity increasing and number concentration decreasing substantially more rapidly than observed between 8 and 6 km (see Figs. 10 and 17).

Simulation biases require dedicated efforts to examine, but appear amenable to progress. For instance, in a follow-on study of this 20 May case (van Lier-Walqui et al., 2016b), we examine the stratiform column processes in isolation using a one-dimensional modeling approach to make a statistical determination of ice crystal properties and aggregation sticking efficiencies; for that work, the KAZR Doppler spectra are found to be essentially free from turbulence broadening in the quiescent stratiform environment, yielding copious information on ice size distribution variation over large regions of stratiform outflow. If outflow ice size distributions aloft are as similar to those present in detraining updrafts as suggested by HAIC/HIWC data from Darwin (at least for ice not sedimented rapidly within updrafts and prior to any substantial aggregation in the outflow), then the 20 May case study is also well suited to study of updraft microphysics.

Case studies are generally better for model development if they are relatively typical rather than unusual or rare. Based on combined analysis of S-band (NEXRAD) and C-band dual-polarimetric radar signatures over several sites and seasons, it has been noted that the 20 May stratiform ice precipitation lacked the positive differential radar reflectivity commonly found in midlatitude stratiform precipitation containing plate-like and oriented crystals (Williams et al., 2015). Williams et al. (2015) report a general absence of robust positive differential reflectivity in the trailing stratiform regions of "vigorous summer squall lines" and attribute that speculatively to the combined effects of irregular ice crystals and stronger electric fields. Strong electric fields have been associated with chain aggregates (e.g., Connolly et al., 2005), which to our knowledge were not profuse over the heavy stratiform rain region in the 20 May case. However, compact and irregular crystals and aggregates are consistent with the available particle images, suggesting that lack of differential reflectivity signature may be indicative of a common stratiform microphysics regime across tropical mesoscale convective systems and midlatitude summer squall lines. The 20 May case therefore could be relatively typical of midlatitude conditions within such a regime.

Analyses of dual-polarimetric radar observations could be further systematically employed to identify the environmental conditions associated with stratiform microphysics regimes, assuming some variety exists, as has been suggested by Leroy et al. (2017). In this 20 May case, analysis of dual-polarimetric radar signatures from C-SAPR and KVNX using the quasi-vertical profile technique during stratiform rain (Kumjian et al., 2016; Ryzhkov et al., 2016) has yielded conclusions generally consistent with the ice properties and microphysical pathways discussed. A high specific differential phase in the absence of differential reflectivity enhancements in the elevation range examined here is consistent with relatively high ice number concentrations and the associated propensity for an active aggregation process despite an absence of dendritic growth. A strong negative gradient in differential reflectivity with elevation above the melting layer is indicative of efficient aggregation; we note that this is most intense approaching the melting level. However, the gradient changes sign near the uppermost elevations sampled by aircraft and examined here (cf. Kumjian et al., 2016, their Fig. 4), so we do not interpret this as conclusive evidence that aggregation is the primary process dominating the ice size distribution shape evolution colder than $-10\,^{\circ}\mathrm{C}$. Finally, within the melting layer, very high differential reflectivity and anomalously high backscatter differential phase are another indication of efficient aggregation above the melting layer (Trömel et al., 2014; Ryzhkov et al., 2016), confirmed by in situ observation of aggregates with $D_{\max}$ greater than 17 mm just above it (not shown).

Owing to the importance of tropical stratiform ice to global circulation, as discussed in Sect. 1, the dominant microphysics regime seen so far in HAIC/HIWC and some past measurements (Leroy et al., 2017), similar to that in the 20 May case, could be among those most important to properly represent in climate models. Aerosol interactions with convection could also be strongly dependent on the microphysics pathways active within a regime. If a warm-temperature ice multiplication mechanism is dominating outflow ice distributions in a manner that cannot be generally reproduced in simulations and is not well understood, it is difficult to confidently assess how or to what degree hygroscopic and ice-nucleating aerosols can be expected to modulate outflow ice properties. For instance, in this study we cannot be confident about the relevance of our sensitivity tests for understanding natural convective outflow, owing to inadequate baseline fidelity compared with observations. Establishing how typical the 20 May case study is may clarify what other case study conditions could be complementary or more relevant for the purposes of model development. With respect to hygroscopic aerosol, from the perspective of CCN concentrations ($2000\,\mathrm{cm}^{-3}$ at $\sim 1\,\%$ supersaturation), the 20 May case is relatively polluted (see Fig. 3).

This is not the first MC3E convection modeling study to conclude that ice microphysics is not yet well represented across microphysics schemes (e.g., Pu and Lin, 2015). Stratiform outflow from deep convection has also been previously identified as an area where different microphysics schemes in cloud-resolving or convection-permitting simulations produce particularly diverse results (e.g., Morrison et al., 2012; Varble et al., 2014b), with substantial associated impacts on

simulated radiative fluxes (e.g., Fridlind et al., 2012; Wang et al., 2015b). Soundly advancing understanding of aerosol effects on deep convection requires better establishing and successfully reproducing in simulations the primary microphysical pathways operating under various environmental conditions. Identifying regimes where similar and distinct microphysical conditions can be identified in observations could usefully advance understanding and model development.

Code availability. Aerosol analysis codes are available in Interactive Data Language on request. The ice size distributions reported by Wu and McFarquhar (2016) were processed using the University of Illinois Optical Array Probe Processing Software (UIOPS), which is open-source software available from https://github.com/weiwu5/UIOPS. NU-WRF software is available from http://nuwrf.gsfc.nasa.gov.

Data availability. Reported aircraft data are available from the DOE ARM program field campaign archive (https://www.arm.gov/research/campaigns/sgp2011midlatcloud) and the NASA Precipitation Measurement Mission Ground Validation program archive (https://pmm.nasa.gov/science/ground-validation). Based on the raw aircraft microphysical measurements (Delene and Poellot, 2013), the ice number and mass size distributions derived as reported by Wang et al. (2015a) and Wu and McFarquhar (2016) are available on request. Ground-based aerosol data are available from the DOE ARM program instrument data stream archive (https://www.arm.gov/capabilities/instruments). The C-SAPR quantitative precipitation estimate is available from the DOE ARM program as an evaluation product (https://www.arm.gov/capabilities/vaps). NEXRAD measurements are available from the US government archive (http://catalog.data.gov/dataset). Specific differential phase and drop size distribution parameters calculated from NEXRAD measurements are available on request. NU-WRF simulations are also available on request.

The Supplement related to this article is available online at doi:10.5194/acp-17-5947-2017-supplement.

Author contributions. Ann M. Fridlind prepared the aerosol data analysis. Xiaowen Li and Di Wu modified NU-WRF to use derived input aerosol specifications, with the assistance of Andrew S. Ackerman. Di Wu ran NU-WRF simulations and compared results with in situ microphysics and precipitation observations. Marcus van Lier-Walqui prepared analysis of observed and simulated radar reflectivity, wind fields, and rain size distribution parameters. Greg M. McFarquhar, Wei Wu, Xiquan Dong, and Jingyu Wang provided airborne cloud microphysics measurements. Alexander Ryzhkov and Pengfei Zhang provided rain size distribution parameter retrievals. Michael R. Poellot, Andrea Neumann, and Jason M. Tomlinson provided airborne aerosol measurements. Ann M. Fridlind and Wei-Kuo Tao coordinated this project with companion studies.

Competing interests. The authors declare that they have no conflict of interest.

Acknowledgements. This work was supported by the Office of Science (BER), US Department of Energy, under agreements DE-SC0006988, DE-SC0014065, and DE-SC0016476 (through UCAR subcontract Z17-90029), and by the NASA Radiation Sciences Program. All measurements were obtained from the Atmospheric Radiation Measurement (ARM) Program sponsored by the US Department of Energy, Office of Science, Office of Biological and Environmental Research, Climate and Environmental Sciences Division. Operation of the University of North Dakota *Citation* aircraft was supported through NASA grant NNX10AN38G. NU-WRF is supported by the NASA Modeling, Analysis and Prediction (MAP) program. Resources supporting this work were provided by the NASA High-End Computing (HEC) Program through the NASA Advanced Supercomputing (NAS) Division at Ames Research Center and NASA's Center for Climate Simulation (NCCS) at Goddard Space Flight Center. We thank Tami Toto and Andrew Vogelmann for supplying their algorithm for fitting multiple lognormal modes to a measured aerosol number size distribution. We thank two anonymous referees for insightful comments that greatly improved the manuscript.

Edited by: C. Hoose
Reviewed by: two anonymous referees

References

Abdul-Razzak, H. and Ghan, S. J.: A parameterization of aerosol activation: 2. Multiple aerosol types, J. Geophys. Res., 105, 6837–6844, 2000.

Ackerman, A. S., Fridlind, A. M., Grandin, A., Dezitter, F., Weber, M., Strapp, J. W., and Korolev, A. V.: High ice water content at low radar reflectivity near deep convection – Part 2: Evaluation of microphysical pathways in updraft parcel simulations, Atmos. Chem. Phys., 15, 11729–11751, doi:10.5194/acp-15-11729-2015, 2015.

Altaratz, O., Koren, I., Remer, L. A., and Hirsch, E.: Review: Cloud invigoration by aerosols – Coupling between microphysics and dynamics, Atmos. Res., 140–141, 38–60, doi:10.1016/j.atmosres.2014.01.009, 2014.

Avramov, A., Ackerman, A. S., Fridlind, A. M., van Diedenhoven, B., Botta, G., Aydin, K., Verlinde, J., Korolev, A. V., Strapp, J. W., McFarquhar, G. M., Jackson, R., Brooks, S. D., Glen, A., and Wolde, M.: Toward ice formation closure in Arctic mixed-phase boundary layer clouds during ISDAC, J. Geophys. Res., 116, D00T08, doi:10.1029/2011JD015910, 2011.

Baker, B. and Lawson, R. P.: Improvement in determination of ice water content from two-dimensional particle imagery. Part I: Image-to-mass relationships, J. Appl. Meteorol. Clim., 45, 1282–1290, 2006.

Barnes, H. C. and Houze Jr., R. A.: Comparison of observed and simulated spatial patterns of ice microphysical processes in tropical oceanic mesoscale convective systems, J. Geophys. Res., 121, 8269–8296, doi:10.1002/(ISSN)2169-8996, 2016.

Barth, M. C., Kim, S.-W., Wang, C., Pickering, K. E., Ott, L. E., Stenchikov, G., Leriche, M., Cautenet, S., Pinty, J.-P., Barthe, Ch., Mari, C., Helsdon, J. H., Farley, R. D., Fridlind, A. M., Ackerman, A. S., Spiridonov, V., and Telenta, B.: Cloud-scale model intercomparison of chemical constituent transport in deep convection, Atmos. Chem. Phys., 7, 4709–4731, doi:10.5194/acp-7-4709-2007, 2007.

Baumgardner, D., Brenguier, J.-L., Bucholtz, A., Coe, H., DeMott, P., Garrett, T. J., Gayet, J. F., Hermann, M., Heymsfield, A., Korolev, A., Krämer, M., Petzold, A., Strapp, W., Pilewskie, P., Taylor, J., Twohy, C., Wendisch, M., Bachalo, W., and Chuang, P.: Airborne instruments to measure atmospheric aerosol particles, clouds and radiation: A cook's tour of mature and emerging technology, Atmos. Res., 102, 10–29, doi:10.1016/j.atmosres.2011.06.021, 2011.

Bigg, E. K.: The supercooling of water, Proc. Phys. Soc. London B, 66, 688–694, 1953.

Biggerstaff, M. and Houze Jr., R. A.: Kinematic and precipitation structure of the 10-11 June 1985 squall line, Mon. Weather Rev., 119, 3034–3065, 1991.

Connolly, P. J., Saunders, C. P. R., Gallagher, M. W., Bower, K. N., Flynn, M. J., Choularton, T. W., Whiteway, J., and Lawson, R. P.: Aircraft observations of the influence of electric fields on the aggregation of ice crystals, Q. J. Roy. Meteor. Soc., 131, 1695–1712, doi:10.1256/qj.03.217, 2005.

Cooper, W. A.: Ice initiation in natural clouds, in: Precipitation Enhancement – A Scientific Challenge, edited by: Braham Jr., R., p. 171, American Meteorological Society, Boston, MA, 1986.

Corr, C. A., Ziemba, L. D., and Scheuer, E.: Observational evidence for the convective transport of dust over the central United States, J. Geophys. Res., 121, 1306–1319, doi:10.1002/2015JD023789, 2016.

Crippa, P. and Pryor, S. C.: Spatial and temporal scales of new particle formation events in eastern North America, Atmos. Environ., 75, 257–264, doi:10.1016/j.atmosenv.2013.04.051, 2013.

D'Adderio, L. P., Porcù, F., and Tokay, A.: Identification and analysis of collisional breakup in natural rain, J. Atmos. Sci., 72, 3404–3416, doi:10.1175/JAS-D-14-0304.1, 2015.

Delene, D. and Poellot, M.: GPM Ground Validation UND Citation Cloud Microphysics MC3E, NASA EOSDIS Global Hydrology Resource Center Distributed Active Archive Center, Huntsville, AL, USA, http://ghrc.nsstc.nasa.gov (last access: 5 April 2012), doi:10.5067/GPMGV/MC3E/MULTIPLE/DATA201, 2013.

DeMott, P. J., Rogers, D. C., Kreidenweis, S. M., Chen, Y., Twohy, C., Baumgardner, D., Heymsfield, A. J., and Chan, K. R.: The role of heterogeneous freezing nucleation in upper troposphereic clouds: Inferences from SUCCESS, Geophys. Res. Lett., 25, 1387–1390, 1998.

DeMott, P. J., Prenni, A. J., Liu, X., Kreidenweis, S. M., Petters, M. D., Twohy, C. H., Richardson, M. S., Eidhammer, T., and Rogers, D. C.: Predicting global atmospheric ice nuclei distributions and their impacts on climate, P. Natl. Acad. Sci. USA, 107, 11217–11222, doi:10.1073/pnas.0910818107, 2010.

Dezitter, F., Grandin, A., Brenguier, J.-L., Hervy, F., Schlager, H., Villedieu, P., and Zalamansky, G.: HAIC – High Altitude Ice Crystals, in: 5th AIAA Atmospheric and Space Environments Conference, American Institute of Aeronautics and Astronautics, Reston, Virginia, doi:10.2514/6.2013-2674, 2013.

Donner, L. J., O'Brien, T. A., Rieger, D., Vogel, B., and Cooke, W. F.: Are atmospheric updrafts a key to unlocking climate forcing and sensitivity?, Atmos. Chem. Phys., 16, 12983–12992, doi:10.5194/acp-16-12983-2016, 2016.

Ekman, A., Wang, C., Ström, J., and Krejci, R.: Explicit simulation of aerosol physics in a cloud-resolving model: Aerosol transport and processing in the free troposphere, J. Atmos. Sci., 63, 682–696, 2006.

Elsaesser, G. S., Del Genio, A. D., Jiang, J. H., and Van Lier-Walqui, M.: An improved convective ice parameterization for the NASA GISS global climate model and impacts on cloud ice simulation, J. Climate, 30, 317–336, doi:10.1175/JCLI-D-16-0346.1, 2017.

Endo, S., Fridlind, A. M., Lin, W., Vogelmann, A. M., Toto, T., Ackerman, A. S., McFarquhar, G. M., Jackson, R. C., Jonsson, H. H., and Liu, Y.: RACORO continental boundary layer cloud investigations: 2. Large-eddy simulations of cumulus clouds and evaluation with in situ and ground-based observations, J. Geophys. Res., 120, 5993–6014, 2015.

Fan, J., Liu, Y.-C., Xu, K.-M., North, K., Collis, S., Dong, X., Zhang, G. J., Chen, Q., Kollias, P., and Ghan, S. J.: Improving representation of convective transport for scale-aware parameterization: 1. Convection and cloud properties simulated with spectral bin and bulk microphysics, J. Geophys. Res., 120, 3485–3509, doi:10.1002/(ISSN)2169-8996, 2015.

Fridlind, A. M., Ackerman, A. S., Jensen, E. J., Heymsfield, A. J., Poellot, M. R., Stevens, D. E., Wang, D., Miloshevich, L., Baumgardner, D., and Lawson, R. P.: Evidence for the predominance of mid-tropospheric aerosols as subtropical anvil cloud nuclei, Science, 304, 718–722, 2004.

Fridlind, A. M., Ackerman, A. S., McFarquhar, G. M., Zhang, G., Poellot, M. R., DeMott, P. J., Prenni, A. J., and Heymsfield, A. J.: Ice properties of single-layer stratocumulus during the Mixed-Phase Arctic Cloud Experiment: 2. Model results, J. Geophys. Res., 112, D24202, doi:10.1029/2007JD008646, 2007.

Fridlind, A. M., Ackerman, A. S., Chaboureau, J.-P., Fan, J., Grabowski, W. W., Hill, A. A., Jones, T. R., Khaiyer, M. M., Liu, G., Minnis, P., Morrison, H., Nguyen, L., Park, S., Petch, J. C., Pinty, J. P., Schumacher, C., Shipway, B. J., Varble, A. C., Wu, X., Xie, S., and Zhang, M.: A comparison of TWP-ICE observational data with cloud-resolving model results, J. Geophys. Res., 117, D05204, doi:10.1029/2011JD016595, 2012.

Fridlind, A. M., Ackerman, A. S., Grandin, A., Dezitter, F., Weber, M., Strapp, J. W., Korolev, A. V., and Williams, C. R.: High ice water content at low radar reflectivity near deep convection – Part 1: Consistency of in situ and remote-sensing observations with stratiform rain column simulations, Atmos. Chem. Phys., 15, 11713–11728, doi:10.5194/acp-15-11713-2015, 2015.

Grandin, A., Merle, J.-M., Weber, M., Strapp, J., Protat, A., and King, P.: AIRBUS flight tests in high total water content regions, in: 6th AIAA Atmospheric and Space Environments Conference, American Institute of Aeronautics and Astronautics, Reston, Virginia, doi:10.2514/6.2014-2753, 2014.

Grim, J. A., McFarquhar, G. M., Rauber, R. M., Smith, A. M., and Jewett, B. F.: Microphysical and thermodynamic structure and evolution of the trailing stratiform regions of mesoscale convective systems during BAMEX. Part II: Column model simulations, Mon. Weather Rev., 137, 1186–1205, doi:10.1175/2008MWR2505.1, 2009.

Hallett, J. and Mossop, S. C.: Production of secondary ice particles during the riming process, Nature, 249, 26–28, 1974.

Heymsfield, A. J.: Properties of tropical and midlatitude ice cloud particle ensembles. Part I: Median mass diameters and terminal velocities, J. Atmos. Sci., 60, 2573–2591, 2003.

Houze, Jr., R. A.: Mesoscale convective systems, Rev. Geophys., 42, 1–43, doi:10.1029/2004RG000150, 2004.

Jensen, M. P., Toto, T., Troyan, D., Ciesielski, P. E., Holdridge, D., Kyrouac, J., Schatz, J., Zhang, Y., and Xie, S.: The Midlatitude Continental Convective Clouds Experiment (MC3E) sounding network: operations, processing and analysis, Atmos. Meas. Tech., 8, 421–434, doi:10.5194/amt-8-421-2015, 2015.

Jensen, M. P., Petersen, W. A., Bansemer, A., Bharadwaj, N., Carey, L. D., Cecil, D. J., Collis, S. M., Del Genio, A. D., Dolan, B., Gerlach, J., Giangrande, S. E., Heymsfield, A., Heymsfield, G., Kollias, P., Lang, T. J., Nesbitt, S. W., Neumann, A., Poellot, M., Rutledge, S. A., Schwaller, M., Tokay, A., Williams, C. R., Wolff, D. B., Xie, S., and Zipser, E. J.: The Midlatitude Continental Convective Clouds Experiment (MC3E), B. Am. Meteorol. Soc., 97, 1667–1686, doi:10.1175/BAMS-D-14-00228.1, 2016.

Khain, A. P., Phillips, V., Benmoshe, N., and Pokrovsky, A.: The role of small soluble aerosols in the microphysics of deep maritime clouds, J. Atmos. Sci., 69, 2787–2807, doi:10.1175/2011JAS3649.1, 2012.

Kumjian, M. R., Mishra, S., Giangrande, S. E., Toto, T., Ryzhkov, A. V., and Bansemer, A.: Polarimetric radar and aircraft observations of saggy bright bands during MC3E, J. Geophys. Res., 121, 3584–3607, doi:10.1002/2015JD024446, 2016.

Ladino, L. A., Korolev, A., Heckman, I., Wolde, M., Fridlind, A. M., and Ackerman, A. S.: On the role of ice-nucleating aerosol in the formation of ice particles in tropical mesoscale convective systems, Geophys. Res. Lett., 44, 1574–1582, doi:10.1002/2016GL072455, 2017.

Lance, S., Brock, C. A., Rogers, D., and Gordon, J. A.: Water droplet calibration of the Cloud Droplet Probe (CDP) and in-flight performance in liquid, ice and mixed-phase clouds during ARCPAC, Atmos. Meas. Tech., 3, 1683–1706, doi:10.5194/amt-3-1683-2010, 2010.

Lawson, R. P., Angus, L. J., and Heymsfield, A. J.: Cloud particle measurements in thunderstorm anvils and possible weather threat to aviation, J. Aircraft, 35, 113–121, 1998.

Lawson, R. P., Jensen, E., Mitchell, D. L., Baker, B., Mo, Q., and Pilson, B.: Microphysical and radiative properties of tropical clouds investigated in TC4 and NAMMA, J. Geophys. Res., 115, D00J08, doi:10.1029/2009JD013017, 2010.

Lawson, R. P., Woods, S., and Morrison, H.: The microphysics of ice and precipitation development in tropical cumulus clouds, J. Atmos. Sci., 72, 2429–2445, doi:10.1175/JAS-D-14-0274.1, 2015.

Lebo, Z. J. and Morrison, H.: Effects of horizontal and vertical grid spacing on mixing in simulated squall lines and implications for convective strength and structure, Mon. Weather Rev., 143, 4355–4375, doi:10.1175/MWR-D-15-0154.1, 2015.

Leroy, D., Fontaine, E., Schwarzenboeck, A., Strapp, J. W., Lilie, L., Delanoë, J., Protat, A., Dezitter, F., and Grandin, A.: HAIC/HIWC field campaign-specific findings on PSD microphysics in high IWC regions from in situ measurements: Median mass diameters, particle size distribution characteristics and ice crystal shapes, Tech. Rep. 2015-01-2087, SAE International, 2015.

Leroy, D., Fontaine, E., Schwarzenboeck, A., Strapp, J. W., Korolev, A., McFarquhar, G. M., Dupuy, R., Gourbeyre, C., Lilie, L., Protat, A., Delanoë, J., Dezitter, F., and Grandin, A.: Ice crystal sizes in high ice water content clouds. Part II: Statistics of mass diameter percentiles in tropical convection observed during the HAIC/HIWC project, J. Atmos. Ocean. Tech., 34, 118–136, doi:10.1175/JTECH-D-15-0246.1, 2017.

Lin, Y., Donner, L. J., Petch, J., Bechtold, P., Boyle, J., Klein, S. A., Komori, T., Wapler, K., Willett, M., Xie, X., Zhao, M., Xie, S., Mcfarlane, S. A., and Schumacher, C.: TWP-ICE global atmospheric model intercomparison: Convection responsiveness and resolution impact, J. Geophys. Res., 117, D09111, doi:10.1029/2011JD017018, 2012.

Liu, C. and Zipser, E. J.: The global distribution of largest, deepest, and most intense precipitation systems, Geophys. Res. Lett., 42, 3591–3595, doi:10.1002/(ISSN)1944-8007, 2015.

Mason, J. G. and Grzych, M.: The challenges identifying weather associated with jet engine ice crystal icing, Tech. Rep. 2011-38-0094, SAE International, Warrendale, PA, doi:10.4271/2011-38-0094, 2011.

Mauritsen, T. and Stevens, B.: Missing iris effect as a possible cause of muted hydrological change and high climate sensitivity in models, Nat. Geosci., 8, 346–351, doi:10.1038/ngeo2414, 2015.

May, P. T., Bringi, V. N., and Thurai, M.: Do we observe aerosol impacts on DSDs in strongly forced tropical thunderstorms?, J. Atmos. Sci., 68, 1902–1910, doi:10.1175/2011JAS3617.1, 2011.

McFarquhar, G. M.: Raindrop size distribution and evolution, Rainfall: State of the Science, 49–60, doi:10.1029/2010GM000971, 2010.

McFarquhar, G. M. and Cober, S.: Single-scattering properties of mixed-phase Arctic clouds at solar wavelengths: Impacts on radiative transfer, J. Climate, 17, 3799–3813, 2004.

McFarquhar, G. M., Timlin, M. S., Rauber, R. M., Jewett, B. F., Grim, J. A., and Jorgensen, D. P.: Vertical variability of cloud hydrometeors in the stratiform region of mesoscale convective systems and bow echoes, Mon. Weather Rev., 135, 3405–3428, doi:10.1175/MWR3444.1, 2007.

Meyers, M. P., DeMott, P. J., and Cotton, W. R.: New primary ice-nucleation parameterizations in an explicit cloud model, J. Appl. Meteorol., 31, 708–721, 1992.

Morrison, H. and Grabowski, W. W.: Modeling supersaturation and subgrid-scale mixing with two-moment bulk warm microphysics, J. Atmos. Sci., 65, 792–812, doi:10.1175/2007JAS2374.1, 2008.

Morrison, H. and Milbrandt, J. A.: Parameterization of cloud microphysics based on the prediction of bulk ice particle properties. Part I: Scheme description and idealized tests, J. Atmos. Sci., 72, 287–311, doi:10.1175/JAS-D-14-0065.1, 2015.

Morrison, H., Thompson, G., and Tatarskii, V.: Impact of cloud microphysics on the development of trailing stratiform precipitation in a simulated squall line: Comparison of one- and two-moment schemes, Mon. Weather Rev., 137, 991–1007, doi:10.1175/2008MWR2556.1, 2009.

Morrison, H., Tessendorf, S. A., Ikeda, K., and Thompson, G.: Sensitivity of a simulated midlatitude squall line to parameterization of raindrop breakup, Mon. Weather Rev., 140, 2437–2460, doi:10.1175/MWR-D-11-00283.1, 2012.

Peters-Lidard, C. D., Kemp, E. M., Matsui, T., Santanello, Jr., J. A., Kumar, S. V., Jacob, J. P., Clune, T., Tao, W.-K., Chin, M., Hou, A., Case, J. L., Kim, D., Kim, K.-M., Lau, W., Liu, Y., Shi, J., Starr, D., Tan, Q., Tao, Z., Zaitchik, B. F., Zavodsky, B., Zhang, S. Q., and Zupanski, M.: Integrated modeling of aerosol, cloud, precipitation and land processes at satellite-resolved scales, Environ. Modell. Softw., 67, 149–159, doi:10.1016/j.envsoft.2015.01.007, 2015.

Pöhlker, M. L., Pöhlker, C., Ditas, F., Klimach, T., Hrabe de Angelis, I., Araújo, A., Brito, J., Carbone, S., Cheng, Y., Chi, X., Ditz, R., Gunthe, S. S., Kesselmeier, J., Könemann, T., Lavric, J. V., Martin, S. T., Mikhailov, E., Moran-Zuloaga, D., Rose, D., Saturno, J., Su, H., Thalman, R., Walter, D., Wang, J., Wolff, S., Barbosa, H. M. J., Artaxo, P., Andreae, M. O., and Püschl, U.: Long-term observations of cloud condensation nuclei in the Amazon rain forest – Part 1: Aerosol size distribution, hygroscopicity, and new model parametrizations for CCN prediction, Atmos. Chem. Phys., 16, 15709–15740, doi:10.5194/acp-16-15709-2016, 2016.

Pu, Z. and Lin, C.: Evaluation of double-moment representation of ice hydrometeors in bulk microphysical parameterization: Comparison between WRF numerical simulationsand UND-Citation data during MC3E, Geosci. Lett., 2, 1–9, doi:10.1186/s40562-015-0028-x, 2015.

Ryzhkov, A., Diederich, M., Zhang, P., and Simmer, C.: Potential utilization of specific attenuation for rainfall estimation, mitigation of partial beam blockage, and radar networking, J. Atmos. Ocean. Tech., 31, 599–619, doi:10.1175/JTECH-D-13-00038.1, 2014.

Ryzhkov, A., Zhang, P., Reeves, H., Kumjian, M., Tschallener, T., Trömel, S., and Simmer, C.: Quasi-vertical profiles – A new way to look at polarimetric radar data, J. Atmos. Ocean. Tech., 33, 551–562, doi:10.1175/JTECH-D-15-0020.1, 2016.

Schumacher, C., Houze Jr., R. A., and Kraucunas, I.: The tropical dynamical response to latent heating estimates derived from the TRMM precipitation radar, J. Atmos. Sci., 61, 1341–1358, 2004.

Smith, A. M., McFarquhar, G. M., Rauber, R. M., Grim, J. A., Timlin, M. S., Jewett, B. F., and Jorgensen, D. P.: Microphysical and thermodynamic structure and evolution of the trailing stratiform regions of mesoscale convective systems during BAMEX. Part I: Observations, Mon. Weather Rev., 137, 1165–1185, doi:10.1175/2008MWR2504.1, 2009.

Stevens, R. G., Pierce, J. R., Brock, C. A., Reed, M. K., Crawford, J. H., Holloway, J. S., Ryerson, T. B., Huey, L. G., and Nowak, J. B.: Nucleation and growth of sulfate aerosol in coal-fired power plant plumes: sensitivity to background aerosol and meteorology, Atmos. Chem. Phys., 12, 189–206, doi:10.5194/acp-12-189-2012, 2012.

Storer, R. L., Van Den Heever, S. C., and Stephens, G. L.: Modeling aerosol impacts on convective storms in different environments, J. Atmos. Sci., 67, 3904–3915, doi:10.1175/2010JAS3363.1, 2010.

Tang, L., Tian, Y., and Lin, X.: Validation of precipitation retrievals over land from satellite-based passive microwave sensors, J. Geophys. Res., 119, 4546–4567, doi:10.1002/2013JD020933, 2014.

Tao, W.-K., Chen, J.-P., Li, Z., Wang, C., and Zhang, C.: Impact of aerosols on convective clouds and precipitation, Rev. Geophys., 50, RG2001, doi:10.1029/2011RG000369, 2012.

Tao, W.-K., Wu, D., Lang, S., Chern, J., Peters-Lidard, C., Fridlind, A., and Matsui, T.: High-resolution NU-WRF simulations of a deep convective-precipitation system during MC3E: Further Improvements and Comparisons between Goddard microphysics schemes and observations, J. Geophys. Res., 121, 1278–1305, doi:10.1002/(ISSN)2169-8996, 2016.

Testud, J., Oury, S., Black, R., Amayenc, P., and Dou, X.: The concept of "normalized" distribution to describe raindrop spectra: A tool for cloud physics and cloud remote sensing, J. Appl. Meteorol., 40, 1118–1140, 2001.

Thompson, G., Rasmussen, R. M., and Manning, K.: Explicit forecasts of winter precipitation using an improved bulk microphysics scheme. Part I: Description and sensitivity analysis, Mon. Weather Rev., 132, 519–542, 2004.

Thurai, M., Bringi, V. N., and May, P. T.: CPOL radar-derived drop size distribution statistics of stratiform and convective rain for two regimes in Darwin, Australia, J. Atmos. Ocean. Tech., 27, 932–942, doi:10.1175/2010JTECHA1349.1, 2010.

Thurai, M., Bringi, V. N., Carey, L. D., Gatlin, P., Schultz, E., and Petersen, W. A.: Estimating the accuracy of polarimetric radar–based retrievals of drop-size distribution parameters and rain rate: An application of error variance separation using radar-derived spatial correlations, J. Hydrometeorol., 13, 1066–1079, doi:10.1175/JHM-D-11-070.1, 2012.

Trömel, S., Ryzhkov, A. V., Zhang, P., and Simmer, C.: Investigations of backscatter differential phase in the melting layer, J. Appl. Meteorol. Clim., 53, 2344–2359, doi:10.1175/JAMC-D-14-0050.1, 2014.

van Lier-Walqui, M., Fridlind, A. M., Ackerman, A. S., Collis, S., Helmus, J. J., MacGorman, D. R., North, K., Kollias, P., and Posselt, D.: Polarimetric radar signatures of deep convection: Columns of specific differential phase observed during MC3E, Mon. Weather Rev., 144, 737–758, doi:10.1175/MWR-D-15-0100.1, 2016a.

van Lier-Walqui, M., Fridlind, A. M., Ackerman, A. S., Williams, C., McFarquhar, G., Wu, W., Li, X., and Korolev, A.: In situ and radar Doppler spectrum constraints of ice sticking efficiency and ice properties in a mid-latitude squall line, International Conference on Clouds and Precipitation, Manchester, UK, 29 July 2016b.

Van Weverberg, K., Vogelmann, A. M., Lin, W., Luke, E. P., Cialella, A., Minnis, P., Khaiyer, M., Boer, E. R., and Jensen, M. P.: The role of cloud microphysics parameterization in the simulation of mesoscale convective system clouds and precipitation in the Tropical Western Pacific, J. Atmos. Sci., 70, 1104–1128, doi:10.1175/JAS-D-12-0104.1, 2013.

Varble, A., Zipser, E. J., Fridlind, A. M., Zhu, P., Ackerman, A. S., Chaboureau, J.-P., Collis, S., Fan, J., Hill, A., and Shipway, B.: Evaluation of cloud-resolving and limited area model intercomparison simulations using TWP-ICE observations: 1. Deep convective updraft properties, J. Geophys. Res., 119, 13891–13918, doi:10.1002/2013JD021371, 2014a.

Varble, A., Zipser, E. J., Fridlind, A. M., Zhu, P., Ackerman, A. S., Chaboureau, J.-P., Fan, J., Hill, A., Shipway, B., and Williams, C.: Evaluation of cloud-resolving and limited area model intercomparison simulations using TWP-ICE observations: 2. Precipitation microphysics, J. Geophys. Res., 119, 13-919–13-945, doi:10.1002/2013JD021372, 2014b.

Vogelmann, A. M., Fridlind, A. M., Toto, T., Endo, S., Lin, W., Wang, J., Feng, S., Zhang, Y., Turner, D. D., Liu, Y., Li, Z., Xie, S., Ackerman, A. S., Zhang, M., and Khairoutdinov, M.: RACORO continental boundary layer cloud investigations: 1. Case study development and ensemble large-scale forcings, J. Geophys. Res., 120, 5962–5992, 2015.

Wang, C.: Impact of anthropogenic absorbing aerosols on clouds and precipitation: A review of recent progresses, Atmos. Res., 122, 237–249, doi:10.1016/j.atmosres.2012.11.005, 2013.

Wang, J., Collins, D., Covert, D., Elleman, R., Ferrare, R. A., Gasparini, R., Jonsson, H., Ogren, J., Sheridan, P., and Tsay, S.-C.: Temporal variation of aerosol properties at a rural continental site and study of aerosol evolution through growth law analysis, J. Geophys. Res., 111, D18203, doi:10.1029/2005JD006704, 2006.

Wang, J., Dong, X., and Xi, B.: Investigation of ice cloud microphysical properties of DCSs using aircraft in situ measurements during MC3E over the ARM SGP site, J. Geophys. Res., 120, 3533–3552, doi:10.1002/2014JD022795, 2015a.

Wang, S., Sobel, A. H., Fridlind, A., Feng, Z., Comstock, J. M., Minnis, P., and Nordeen, M. L.: Simulations of cloud-radiation interaction using large-scale forcing derived from the CINDY/DYNAMO northern sounding array, J. Adv. Model. Earth Syst., 7, 1472–1498, doi:10.1002/2015MS000461, 2015b.

Westerdahl, D., Fruin, S. A., Fine, P. L., and Sioutas, C.: The Los Angeles International Airport as a source of ultrafine particles and other pollutants to nearby communities, Atmos. Environ., 42, 3143–3155, doi:10.1016/j.atmosenv.2007.09.006, 2008.

Williams, C. R.: Reflectivity and liquid water content vertical decomposition diagrams to diagnose vertical evolution of raindrop size distributions, J. Atmos. Ocean. Tech., 33, 579–595, doi:10.1175/JTECH-D-15-0208.1, 2016.

Williams, E. R., Smalley, D. J., Donovan, M. F., Hallowell, R. G., Hood, K. T., Bennett, B. J., Evaristo, R., Stepanek, A., Bals-Elsholz, T., Cobb, J., Ritzman, J., Korolev, A., and Wolde, M.: Measurements of differential reflectivity in snowstorms and warm season stratiform systems, J. Appl. Meteorol. Clim., 54, 573–595, doi:10.1175/JAMC-D-14-0020.1, 2015.

Wu, W. and McFarquhar, G. M.: On the impacts of different definitions of maximum dimension for nonspherical particles recorded by 2D imaging probes, J. Atmos. Ocean. Tech., 33, 1057–1072, doi:10.1175/JTECH-D-15-0177.1, 2016.

Yang, Q., Easter, R. C., Campuzano-Jost, P., Jimenez, J. L., Fast, J. D., Ghan, S. J., Wang, H., Berg, L. K., Barth, M. C., Liu, Y., Shrivastava, M. B., Singh, B., Morrison, H., Fan, J., Ziegler, C. L., Bela, M., Apel, E., Diskin, G. S., Mikoviny, T., and Wisthaler, A.: Aerosol transport and wet scavenging in deep convective clouds: A case study and model evaluation using a multiple passive tracer analysis approach, J. Geophys. Res., 120, 8448–8468, 2015.

Zeng, X., Tao, W., Matsui, T., Xie, S., Lang, S., Zhang, M., Starr, D., and Li, X.: Estimating the ice crystal enhancement factor in the tropics, J. Atmos. Sci., 68, 1424–1434, doi:10.1175/2011JAS3550.1, 2011.

Zhang, J., Howard, K., Langston, C., Vasiloff, S., Kaney, B., Arthur, A., Van Cooten, S., Kelleher, K., Kitzmiller, D., Ding, F., Seo, D.-J., Wells, E., and Dempsey, C.: National Mosaic and Multi-Sensor QPE (NMQ) system: Description, results, and future plans, B. Am. Meteorol. Soc., 92, 1321–1338, doi:10.1175/2011BAMS-D-11-00047.1, 2011.

Zhu, P., Dudhia, J., Field, P. R., Wapler, K., Fridlind, A., Varble, A., Zipser, E., Petch, J., Chen, M., and Zhu, Z.: A limited area model (LAM) intercomparison study of a TWP-ICE active monsoon mesocale convective event, J. Geophys. Res., 117, D11208, doi:10.1029/2011JD016447, 2012.